ISSN 0252-1075
Contribution from IITM
Research Report No. RR-148
ESSO/IITM/CVP /SR/01(2026)/206

IITM Decadal Climate Prediction System (IITM-DCPSv1): Representation of Interannual to Decadal Climate Variability and Indian Summer Monsoon Teleconnections

P. V. Rajesh[1], Rosimitha Panda[1], C. Gnanaseelan[1]*, Rahul Pai[1,2], Rashmi Kakatkar[1], Darshana Patekar[1], J.S. Deepa[1], A.G. Prajeesh[1,3], Amit Kumar Sharma[1], T.S. Fousiya[1,4], Subrota Halder[1,2], Anila Sebastian[1], Anant Parekh[1], Saikat Pramanik[1]

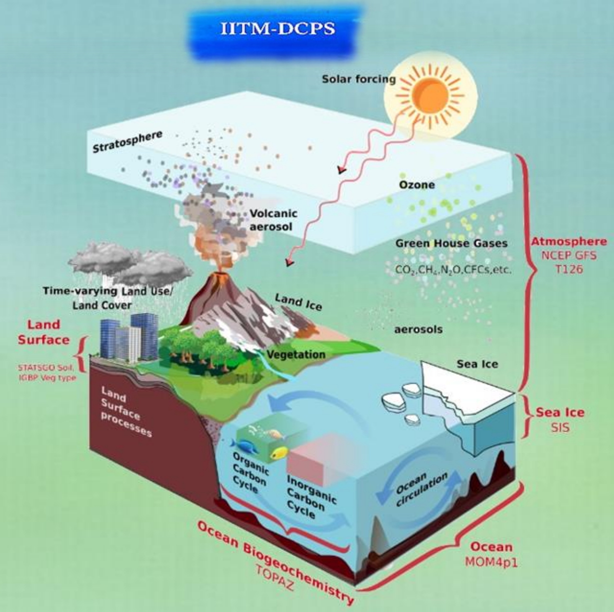

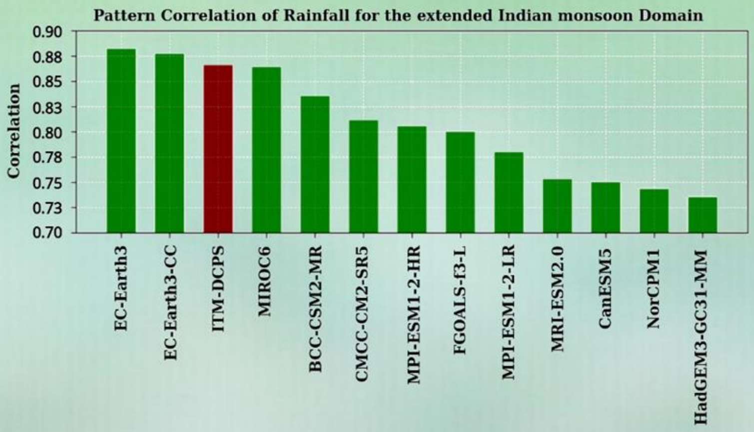

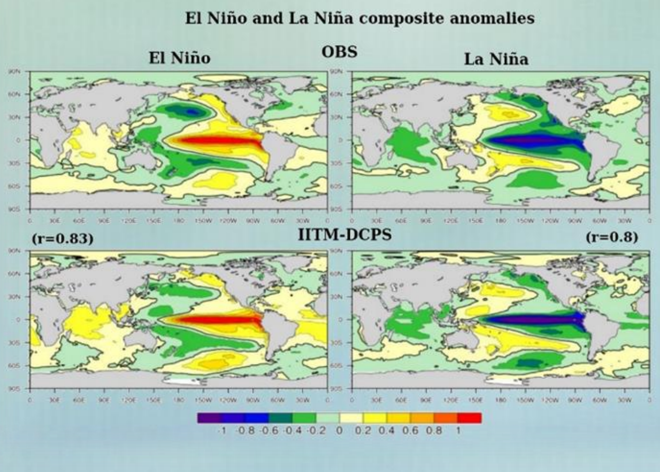

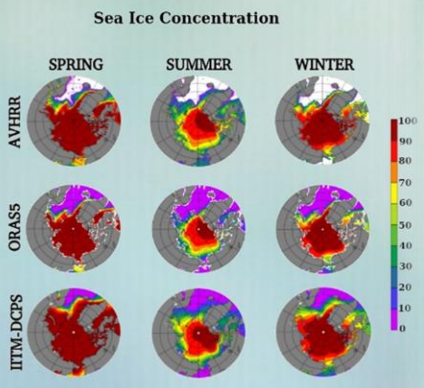

Indian Institute of Tropical Meteorology (IITM)
Ministry of Earth Sciences (MoES)
PUNE, INDIA
https://www.tropmet.res.in/

ISSN 0252-1075
Contribution from IITM
Research Report No. RR-148
ESSO/IITM/CVP /SR/01(2026)/206

IITM Decadal Climate Prediction System (IITM-DCPSv1): Representation of Interannual to Decadal Climate Variability and Indian Summer Monsoon Teleconnections

P. V. Rajesh[1], Rosimitha Panda[1], C. Gnanaseelan[1]*, Rahul Pai[1,2], Rashmi Kakatkar[1],
Darshana Patekar[1], J.S. Deepa[1], A.G. Prajeesh[1,3], Amit Kumar Sharma[1], T.S. Fousiya[1,4],
Subrota Halder[1,2], Anila Sebastian[1], Anant Parekh[1], Saikat Pramanik[1]

[1] Climate Variability and Prediction, Indian Institute of Tropical Meteorology, Ministry of Earth Sciences, Pune 411 008 India.
[2] New York University Abu Dhabi, UAE.
[3] CECI/CERFACS Toulouse, France.
[4] King Abdullah University of Science and Technology, Saudi Arabia.

***Corresponding Author:**
Dr. C. Gnanaseelan
Scientist G and Project Director
Climate Variability and Prediction (CVP)
Indian Institute of Tropical Meteorology,
Dr. Homi Bhabha Road, Pashan, Pune-411 008, India.
E-mail: seelan@tropmet.res.in
Phone: +91 -(0)20-259 04 271

Indian Institute of Tropical Meteorology (IITM)
Ministry of Earth Sciences (MoES)
PUNE, INDIA
https://www.tropmet.res.in/

DOCUMENT CONTROL SHEET

Ministry of Earth Sciences (MoES)
Indian Institute of Tropical Meteorology (IITM)

ESSO Document Number
ESSO/IITM/CVP /SR/01(2026)/206

Title of the Report
IITM Decadal Climate Prediction System (IITM-DCPSv1): Representation of Interannual to Decadal Climate Variability and Indian Summer Monsoon Teleconnections.

Authors
P. V. Rajesh, Rosimitha Panda, C. Gnanaseelan*, Rahul Pai, Rashmi Kakatkar, Darshana Patekar, J.S. Deepa, A.G. Prajeesh, Amit Kumar Sharma, T.S. Fousiya, Subrota Halder, Anila Sebastian, Anant Parekh, Saikat Pramanik

Reviewers
Dr. Ayantika Dey Choudhury
[Indian Institute of Tropical Meteorology, Pune]
Dr. K. Ashok
[Professor, CEOAS, University of Hyderabad, Hyderabad]

Type of Document
Scientific Report

Number of pages and figures
55, 22

Number of references
161

Keywords
Decadal Prediction, IITM-DCPS, Global teleconnections, Indian Summer Monsoon

Security classification
Open

Distribution
Unrestricted

Date of Publication
February 2026

Abstract:

This study evaluates the performance of the Indian Institute of Tropical Meteorology (IITM) Decadal Climate Prediction System (IITM-DCPS), developed from the version 1 of IITM Earth System Model (ESMv1) for decadal climate prediction and to contribute towards the Decadal Climate Prediction Project (DCPP). The model incorporates heterogeneous land surface characteristics, including soil types derived from the STASGO/FAO dataset and vegetation types from the USGS dataset, together with vegetation-based surface roughness parameterizations. Land-atmosphere coupling is further improved through the integration of the 2017 physics updates of the Global Forecast System (GFS), along with enhanced static fields such as deep soil temperature, surface roughness length, orography, surface emissivity, soil and vegetation type datasets, aerosols, greenhouse gas forcings, ozone, solar forcing, and vegetation fraction. These enhancements collectively contribute to improved simulation accuracy. As the model is aimed to provide accurate climate prediction in the annual to decadal time scale, we first assessed its internal climate variability through a control simulation with fixed forcings, focusing on its ability to capture the interannual to low-frequency climate variability and its skill in simulating the South Asian monsoon system, including its global teleconnections. The salient features of IITM-DCPS include less biases in mid-latitude temperature compared to most of the global climate models, realistic representation of the annual precipitation cycle over India especially in the core monsoon region. Realistic variances in intraseasonal oscillations, simulation of monsoon wind fields, and tropospheric temperature sensitivity to monsoon dynamics further highlight the model's advancements. Additionally, the model accurately captures the dominant climate modes, such as El Nino Southern Oscillation (ENSO), Pacific Decadal Oscillation (PDO), and Atlantic Multidecadal Oscillation (AMO), across multiple timescales, along with stronger dynamical coupling with monsoon circulation. These features collectively strengthen the predictive capabilities of IITM-DCPS and in particular the South Asian monsoon and its teleconnections, positioning it as a robust tool for decadal climate prediction.

Summary:

This study evaluates the performance of the Indian Institute of Tropical Meteorology Decadal Climate Prediction System (IITM-DCPS) in simulating interannual to decadal variability of the Indian Summer Monsoon (ISM) and its associated global teleconnections. Compared to its predecessor, IITM-ESM, the IITM-DCPS demonstrates substantial improvements in

representing mean monsoon characteristics and large-scale climate variability. The model significantly reduces mid-latitude temperature biases and improves the spatial distribution of monsoon rainfall, intraseasonal oscillations, and tropospheric temperature gradients, all of which are critical for realistic ISM dynamics. These improvements primarily arise from refined surface-layer physics, updated vegetation and soil classifications, and enhanced horizontal resolution. Together, these upgrades result in more realistic land–atmosphere feedbacks, improved surface energy balance, near-surface temperature fields, and moisture transport processes, leading to better simulation of precipitation and temperature variability.

The IITM-DCPS also shows enhanced skill in capturing major global climate modes such as ENSO, PDO, AMO, and IPO, which modulate ISM variability across multiple timescales. In particular, the model reproduces ENSO–ISM lead–lag relationships and simulates multi-decadal teleconnections such as AMO–ISM and PDO–ISM linkages with reasonable fidelity, including the ~65-year AMO periodicity. However, some systematic biases persist, including the westward extension of ENSO-induced SST anomalies and discrepancies in tropical Indian Ocean SSTs and associated teleconnection structures.

Overall, the IITM-DCPS represents a significant advancement for monsoon research and decadal climate prediction while highlighting areas requiring further refinement, particularly in aerosol–cloud interactions and land-surface processes. Its improved predictive capabilities across multiple timescales make it a valuable tool for the development and implementation of an advanced decadal climate prediction system.

Contents

1. Introduction

Advancing climate science to address the multifaceted challenges of climate variability relies on the continuous refinement of Earth system models (ESMs) to better capture the complexities of the climate system (Guillemot, 2022; Alizadeh, 2022; CCSP, 2008; Hansen et al., 2005). As our understanding of climate dynamics deepens, there is an increasing need to enhance the predictive skill of modelling frameworks to represent intricate global and regional climate processes accurately. A pivotal step in this effort is the development of the first version of Indian Institute of Tropical Meteorology (IITM) decadal climate prediction system (IITM-DCPSv1, hereafter IITM-DCPS), from the first version of the IITM Earth System Model (IITM-ESMv1) (Swapna et al., 2015). IITM-DCPS is a radiatively balanced model, optimized for climate studies, and shows improved simulation of global climate and regional monsoon phenomena. It serves as the core component of India's decadal climate prediction efforts and is designed to meet the objectives of the DCPP within the Coupled Model Intercomparison Project (CMIP6 and CMIP7) frameworks (Boer et al., 2016). Robust prediction of climate variability on decadal timescales is its prime objective.

A critical factor for enhancing the decadal prediction capability is the adoption of higher horizontal resolution in ESMs compared to their coarser-resolution counterparts. High-resolution ESMs significantly improve the simulation of climate processes, particularly the Atmospheric Cloud-Radiative Effect in regions like the Pacific and Atlantic cold tongue, where shallow stratocumulus clouds dominate, due to better representation of longwave radiation and reduced biases (e.g., Lin & Yu, 2022). In contrast, lower-resolution models often struggle to accurately capture the regional climate features, such as extreme precipitation, orographic effects, and vegetation influences (Ajibola & Afolayan, 2024). High-resolution models demonstrate superior performance in simulating convective activity in warm regions (Wehner et al., 2014) and precipitation patterns over areas like Europe, the United States, and Australia.

The benefits of enhanced model resolution extend beyond the atmospheric component to the oceanic component of coupled models. Higher resolution enables more accurate representation of features such as the Gulf Stream, reducing biases in regional dynamic sea level (Li et al., 2022). This improves the simulation of tropical Pacific Sea Surface Temperature (SST) annual cycle, as well as the onset and withdrawal timings of El Niño (Arora, 2023). High-resolution coupled models also better replicate Atlantic Meridional Overturning Circulation (AMOC) pathways, aligning more closely with observations. They also capture variability, such as chaotic-intrinsic variability from mesoscale ocean eddies or near-inertial waves, which cannot be resolved by lower-resolution models.

Beyond model resolution, understanding and predicting specific climate phenomena is a central goal of decadal prediction systems, with significant implications for regional climate. Advancements in coupled ocean-atmosphere models and data-driven approaches highlight significant progress in predicting tropical phenomena such as monsoons, the El Niño Southern Oscillation (ENSO), and the Indian Ocean Dipole (IOD), though challenges persist due to internal climate variability, model biases, and initialization uncertainties. For ENSO, coupled models demonstrate robust predictability beyond one year, with enhanced multi-year skill in forecasting near-surface air temperature and precipitation following El Niño or La Niña events, as linear reduced-gravity ocean models effectively capture thermocline depth variations in the tropical Pacific (Rashid et al., 2020). Predictions of the IOD show emerging multi-year capabilities, with decadal modulations in skill linked to southern hemisphere influences, enabling forecasts beyond two years in advanced systems despite model diversity and biases (Feba et al., 2021). Monsoon predictions, particularly for Asian and West African systems, benefit from CMIP6 hindcasts, which improve accuracy in extreme rainfall frequency, intensity, and spatiotemporal patterns through bias correction and machine learning, although precipitation skill remains lower than temperature forecasts and sensitive to subseasonal dynamics (Liu et al., 2023; Ling et al., 2022; Konda et al., 2023). Multi-model ensembles and physical-statistical hybrids are increasingly critical for enhancing tropical predictability under climate change (Smith et al., 2019). Over the past two decades, initiatives such as the CMIP have played a pivotal role in shaping the landscape of climate research (Carvalho et al, 2022), providing a standardised platform for model evaluation and facilitating multi-model analyses. As CMIP continues to evolve, newer versions such as CMIP6 have ushered in a wealth of data, crucial for understanding past climate trends and projecting future scenarios.

The practical value of decadal prediction lies in its ability to fill a critical gap in climate information across timescales by bridging seasonal forecasts and long-term climate projections (Meehl et al., 2009b), thereby providing skillful predictions that support sectors such as agriculture, water management, and disaster risk reduction. Amidst the undeniable reality of climate change, which now poses profound consequences, significant strides are being made to enhance climate modelling capabilities, especially at decadal timescales. While long-term climate projections offer valuable insights, there's a pressing need for actionable information on shorter-moderate timescales as they predict climate variations over several years to a decade (Bojovic et al., 2019), to support effective decision-making in vulnerable sectors**.** Unlike seasonal forecasts, DCPS integrates observations with climate models (WCRP-Climate, 2023), employing full-field initialization of ocean and atmospheric profiles, including SSTs, to capture internal variability. These systems also incorporate external forcings such as greenhouse gases, aerosols, ozone, solar forcing, and vegetation changes to enhance predictive skill. DCPS's ability to forecast climate on decadal scales shows promise (Befort et al., 2020; Mahmood et al., 2021), offering targeted insights for informed decisions towards a resilient future .

A key challenge in decadal climate prediction is distinguishing the externally forced climate change signal from the system’s inherent internal variability (Meehl et al., 2009; Doblas-Reyes et al., 2013). Beyond assessing predictive skill, decadal prediction also provides a framework to address fundamental science questions, improving our understanding of climate processes, variability across timescales, climate sensitivity, and model development (Meehl et al., 2009). Climate variability arises from processes both external to the Earth's climate system and internal to it, either independently or combination of both (Morales, 2022, IPCC, 2021). The externally forced variations are caused by variations in solar forcing, and anthropogenic changes in greenhouse gas concentrations and aerosol loadings (Meehl et al., 2014). However, the intrinsic climate variability of the Earth system emerges from complex interactions among its components (Deser et al., 2012). This natural variability drives regional-global climate fluctuations across multiple timescales, including interannual (2–7 years), decadal (10–30 years), multidecadal (60–70 years), and centennial periods. Understanding the contributions of this natural internal variability versus anthropogenic forcing is critical for decision-makers across various sectors. They require clarity on whether observed climate events are transient manifestations of natural variability, likely to reverse, or indicative of potentially irreversible changes driven by human-induced climate change. The representation of natural variability arising from the slowly-varying components of the climate system differs considerably among models, so the inherent predictability of the climate system on the decadal time scale is also not well established.

This study presents a comprehensive evaluation of the first version of IITM-DCPS, focusing on a key aspect of its representation of internal climate variability-a major driver of regional climate phenomena and a key source of uncertainty in decadal climate prediction. Our analysis systematically assesses the model’s biases, variance, and spatial-temporal correlations against observations, with particular emphasis on the teleconnections of the Indian Summer Monsoon Rainfall (ISMR). Through this detailed evaluation, we aim to clarify the potential predictability of IITM-DCPS and contribute to the broader advancement of climate modelling and decadal prediction capabilities.

2. Data and Methodology

2.1 Validation Datasets

The performance of IITM-DCPS was evaluated against multiple observational and reanalysis datasets spanning key climate variables such as temperature, precipitation, and SST, which were further used to calculate climate and circulation indices over global as well as regional domains. 2m (surface) temperature climatology and atmospheric circulation indices were validated against ERA5 reanalysis (Hersbach et al., 2020), while acknowledging its higher uncertainty during the pre-satellite era due to sparse observations. Global precipitation climatology was assessed using the Global Precipitation Climatology Project (GPCP) version 2 dataset (Adler et al., 2003), and regional precipitation over India was validated against the high-resolution gridded rainfall dataset from the India Meteorological Department (IMD; Pai et al., 2014; Rajeevan et al., 2006), with recognition of uncertainties related to gauge density and under catch, particularly in earlier periods (Sun et al., 2018). SST climatology and all dominant climate modes including ENSO, AMO, and Interdecadal Pacific Oscillation (IPO) were evaluated using the Centennial in situ Observation-Based Estimates (COBE) SST version 2 dataset (Hirahara et al., 2014), with consideration of uncertainties from historical measurement practices and sparse coverage in the pre-satellite era (Kennedy, 2014). While these reference datasets provide robust benchmarks, they are not free from uncertainties, which arise from sparse observational coverage, retrieval and measurement errors, and biases in observational practices or reanalysis methods; these issues are particularly pronounced in the pre-satellite era, when reconstructions relied more heavily on indirect observations or model-based estimates (Merchant et al., 2017; Dell'Aquila et al., 2005). However, it should be noted that for low-frequency climate variability modes such as the AMO or PDO, the impact of data sparsity is relatively less important, since their spatial structures extend over large regions and can often be captured even with limited observational sampling (Trenberth and Shea, 2006) All datasets, along with model outputs, were regridded to a common 1° × 1° grid using bilinear interpolation to ensure consistent spatial comparison.

2.2 Overview of the IITM-DCPS

In pursuit of advancing climate modelling capabilities, we have developed the IITM-DCPS by transforming the IITM-ESM. The IITM-DCPS incorporates refined parameterizations, improved model initialization techniques (3D-variational Grid point Statistical Interpolation on Global Forecast System (GFS) and systematic nudging the temperature profiles towards Ocean Reanalysis System 5 (ORAS5) on MOM4p1), and key updates to the surface layer physics mostly adopted from the 2017 GFS update, along with modifications in the land surface model. Collectively, these changes have improved the model's performance, evidenced by accurate simulation of decadal climate variability, significantly less temperature biases and initial drift which are issues common in many climate models (Sanchez et al., 2016; Pasternack et al., 2021). The following details the notable changes implemented in the IITM-DCPS.

The atmospheric component of the IITM-DCPS (Figure 1) is the NCEP GFS model, configured with a spectral triangular truncation of 126 waves (T126), corresponding to an approximately 1° horizontal grid, and 64 sigma-pressure hybrid layers extending to a model top at 0.2 hPa. It employs the simplified Arakawa–Schubert convection scheme, incorporating cumulus momentum mixing to enhance the representation of atmospheric dynamics. The ocean component utilizes the Modular Ocean Model version 4p1 (MOM4p1), with a horizontal resolution of 0.5° zonally and 0.25° meridionally, coarsening poleward of 30°S and 30°N. It includes 40 vertical levels, with 27 concentrated in the upper 400 m, and applies the K-Profile Parameterization (KPP) scheme (Large et al., 1994) for vertical diffusivity, viscosity, and non-local transport, as detailed in Griffies et al. (2009). The sea ice component is the Sea Ice Simulator version 1 (SIS), a coupled model described by Delworth et al. (2006), which represents sea ice as a three-layer system with five-layer thickness categories. Interactive biogeochemistry is integrated via the Tracers of Phytoplankton with Allometric Zooplankton (TOPAZ) module within a generic ocean turbulence framework, enabling comprehensive simulation of ocean and sea-ice dynamics, thermodynamics, and local tracer variations driven by physical and biogeochemical interactions.

Further, IITM-DCPS uses the Noah land surface model (LSM) version 2.7.1, which includes a single-layer snowpack, vegetation, and 4 underlying soil layers. Studies by Saha et al. (2017) have identified biases in snow-covered midlatitude regions that may affect the accuracy of coupled forecasting systems using Noah. To address these limitations while retaining Noah 2.7.1, we modified the surface layer, including momentum and heat transfer exchange constraints adopted from the NCEP-GFS model as a part of their 2017 update (Zheng et al., 2017) and the adoption of STATSGO-19 soil and USGS-24 vegetation classifications to improve land surface processes. Additionally, the model integrates MODIS snow-free albedo fields, incorporating both direct and diffused sea surface albedo, as well as direct MODIS maximum snow albedo in surface albedo schemes. Further modifications include vegetation-based surface roughness parameterizations, tuned Zilitinkevich coefficient (czil) for optimized aerodynamic resistance in land-atmosphere coupling, and high-resolution land surface boundary datasets. Collectively, these changes enhance the model’s ability to mitigate near-surface temperature biases over midlatitude land regions, cold biases in snow-covered areas and warm biases in the Southern Ocean, which are common in most of the climate models, as shown in section 3.

2.3 Description of Control Simulation

The 220 years long control simulation was done with atmospheric trace gas concentrations, anthropogenic aerosols, insolation, and land cover remaining constant at 2005 levels, without interannual variations using the IITM-DCPS. This fixed-forcing experimental design is essential to isolate the model's internal climate variability from externally forced changes. To achieve a quasi-equilibrium state in the beginning, we performed a 30-year spin-up integration in fully coupled mode, initializing the model from a randomized present-day ocean-atmosphere state. The subsequent control simulation establishes a baseline for examining the internal variability of the climate system within the IITM-DCPS framework. The extended period of more than 200 years of simulation enables the characterization of intrinsic variability across multi-decadal to centennial timescales. By maintaining fixed greenhouse gas concentrations, the IITM-DCPS control simulation offers a stable framework to evaluate internal climate variability and the model’s response under quasi-equilibrium conditions.

This study utilizes CMIP6 pre-industrial control (piControl) simulations as a benchmark to assess the IITM-DCPS model's spatial bias patterns and intrinsic variability. It is important to note that the IITM-DCPS simulations use fixed present-day (2005) forcings and so is not a pre-industrial climate simulations. Therefore, this comparison is explicitly not an evaluation of the forced climate response or absolute climatological values. The analysis is designed to isolate basic broader model structural biases and internal variability characteristics, which are considered less dependent on the background forcing state, making the piControl a valid and community-standard reference for these specific diagnostics.

3. Results

3.1 Analysis of Model Equilibrium

The control simulation of the IITM-DCPS under fixed 2005 greenhouse gas concentrations demonstrates that the model attains a quasi-equilibrium climate state in 200 years of integration (Figure 2a-d). The model exhibits minimal long-term drift, with SST (Figure 2a) stabilizing at approximately 17.9°C showing negligible trend and surface air temperature (TAS) (Figure 2b) maintaining a mean of ≈14.05°C with negligible trend. These equilibrium values are comparable to observational estimates for the 2005 period global mean SST of ~16.8-17.2 °C (Rayner et al., 2003) and global mean surface temperature of 14.5-14.7 °C (Morice et al., 2012), though the model remains slightly warmer, consistent with the known warm biases in coupled models, particularly those arising from misrepresentation of Southern Ocean cloud-radiation feedback. The top-of-atmosphere (TOA) (Figure 2c) net radiative flux shows a mean imbalance of +2.02 W/m^2, which gradually diminishes at a rate of -0.0008 W/m^2/yr. While this exceeds contemporary observational estimates of Earth's energy imbalance (~+0.5 to +1.0 W/m^2; Trenberth et al. 2014), the primary requirement for decadal prediction applications is model stability rather than exact radiative equilibrium, as short-term prediction skill (up to 10 years) is determined more by initial conditions and internal variability than by centennial-scale energy balance adjustments. The decomposition of the TOA flux budget (Figure 2d) reveals that this small net imbalance results from stable, offsetting components. The stability of SST, a critical indicator of ocean-atmosphere energy balance combined with negligible atmospheric temperature drift, ensures that the IITM-DCPS does not suffer from substantial climate drift during the forecast periods. Any residual drift is extremely small and well within acceptable limits for CMIP6-class control runs, giving confidence that the variability analyzed in our study predominantly reflects the model's internal climate variability rather than artifacts from model drift.

3.2 Global mean surface fields

Global mean temperature is a key metric for evaluating model performance in simulating climate change and its impacts (Hausfather et al., 2020; Beusch et al., 2020). To understand the baseline state of the global models, we first analyzed the JJAS mean climatological biases of 2m temperature, precipitation and SST of IITM-DCPS along with piControl runs of 12 CMIP6 models that participated in DCPP, with respect to the observed climatology (Figure 3). Focusing on JJAS biases highlights peak monsoon dynamics and the strongest land-sea thermal contrast, revealing systematic model deficiencies often obscured in annual mean diagnostics.. Observational reference climatologies for temperature (NCEP-v3) and SST (ERSST-v3) use the pre-industrial baseline period 1850-1900 for the DCPP models, while IITM-DCPS biases are evaluated against the present-day climatological mean from 1981-2010, to ensure appropriate comparison periods, while acknowledging that precipitation observations (GPCP) are only available from 1979 onward. Our analysis revealed a persistent positive bias over the Southern Ocean in most models (Figure 3a1-m1), a feature widely attributed to deficiencies in simulating shallow convective clouds and shortwave radiation feedback, which lead to Southern Ocean warming (e.g Kay et al., 2016; Swapna et al., 2018). Improvements to ice microphysics schemes have been proposed to mitigate this bias by enhancing Southern Ocean cloud albedo (Varma et al., 2020), while recent studies suggest that warm biases in the North Atlantic deep ocean, driven by adiabatic AMOC processes, may also contribute to such global temperature bias (Luo et al., 2023).

A pronounced warm SST bias (Figure 3a3-m3) over the Southern Ocean evident in models such as CMCC-CM2-SR5, EC-Earth3, EC-Earth3-CC, FGOALS-f3-L, MIROC6, MPI-ESM1-2-HR/LR, MRI-ESM2-0, and IITM-DCPS may be attributed to the underestimation of supercooled liquid cloud cover and excessive shortwave absorption (Bodas-Salcedo et al., 2014; Hyder et al., 2018). This bias weakens the meridional temperature gradient and induces warm TAS biases across the Southern Hemisphere mid-latitudes. In contrast, cold high-latitude land biases over Eurasia and North America appear in BCC-CSM2-MR, EC-Earth3 variants, FGOALS-f3-L and MRI-ESM2-0, possibly linked to excessive snow cover, high surface albedo, and insufficient turbulent mixing under stable boundary-layer conditions (Holtslag et al., 2013; Niu et al., 2011). Several models including FGOALS-f3-L, IITM-DCPS, MIROC6, MPI-ESM1-2-LR/HR, and NorCPM1 exhibit pronounced midlatitude North and South Pacific cold SST biases, consistent with earlier studies linking these biases to excessive surface heat loss, storm-track wind biases, and cloud–radiation errors that reduce shortwave absorption (e.g Hyder et al., 2018; IPCC, 2021). Precipitation biases (Figure 3a2-m2) across the CMIP6 models further reveal structural deficiencies, with nearly all models displaying excessive rainfall over the Maritime Continent and the equatorial warm pool, along with dry biases over the Indian monsoon region particularly in CanESM5, EC-Earth3 variants, FGOALS-f3-L, HadGEM3-GC31-MM, and MRI-ESM2-0. These patterns reflect persistent challenges in simulating convection-orography interactions and monsoon-ITCZ coupling (Schiemann et al., 2014; Hwang et al., 2021). In addition, many models exhibit an exaggerated wet bias over the western Pacific warm pool, associated with an unrealistically warm and expanded Indo-Pacific Warm Pool that could strengthen local ascent and shifts the Walker circulation's ascending branch eastward, thereby intensifying precipitation over the Maritime Continent and adjacent equatorial regions (Li & Xie, 2014; IPCC AR6, 2021)

Comparing with the other ESMs, IITM-DCPS exhibits relatively reduced JJAS rainfall biases over central and northwest India, realistic representation of the Bay of Bengal rainfall maximum, and a more realistic land-sea thermal contrast that develops the monsoon trough. The model also better captures key Indian Ocean features, including reduced warm SST biases in the Arabian Sea and a more realistic east-west gradient across the equatorial Indian Ocean, which together lead to improved moisture transport and monsoon circulation relative to most DCPP models. Further, the Southern Ocean warm bias in the DCPS is significantly low compared to the bias prevalent in EC-Earth and MPI model families, and the representation of the tropical SST structure particularly reducing the cold bias and producing a more realistic monsoon rainfall distribution compared to most of the DCPP models. These improvements can be attributed to a combination of targeted physics advances, including enhanced boundary-layer turbulence formulations, updated soil-vegetation and snow parameterizations, improved air–sea flux coupling (Zheng et al., 2012; 2017), as well as the improved model resolution. The systematic biases across CMIP6 piControl models highlight structural limitations in cloud-radiation interactions, ocean-atmosphere coupling, and monsoon ITCZ dynamics. The reduced biases and improved mean state in IITM-DCPS could provide a suitable baseline for initialized decadal prediction and support a more consistent representation of Indo-Pacific climate processes.

3.3 Improvements in mean Indian Monsoon Simulation

To assess the performance of ESMs in simulating the Indian monsoon, we analyzed the pattern correlation of various ESMs participated in DCPP with the observed (GPCP) monsoon spatial distributions (climatological) over the extended South Asian monsoon domain (40ºE-120ºE, 10ºS-40ºN) (Figure 4) and also the seasonal rainfall cycle (Figure 5) over the core monsoon domain using piControl simulations from 12 climate models that participate in CMIP6 and are included in the DCPP framework, together with the IITM-DCPS. The models shown in green represent the CMIP6 piControl runs, while the IITM-DCPS control run, shown in maroon, is performed with fixed 2005 GHG concentrations. This comparison between CMIP6 pi-control and IITM-DCPS control run with fixed GHG concentrations at 2005 remains valid for evaluating mean rainfall spatial patterns, as the climatological mean of monsoon rainfall is largely governed by internal variability and physical parameterizations, while the relatively small forced trends over the historical period have a negligible impact on the long-term average spatial distribution. Figure 4 shows the skill of IITM-DCPS in simulating mean monsoon climatology, providing a comparative perspective against other DCPP models. Notably, out of the 13 models examined, IITM-DCPS occupies the 3rd position in the descending order of pattern correlation (0.87), indicating a high level of agreement with observed climatological spatial distributions. This represents how well the models capture the wet-dry contrasting pattern over the South Asian monsoon domain, characterized by wet regions in the east and semi-arid regions to the west, as well as the oceanic rainfall features. This pattern analysis provides insights into the models' ability to reproduce the monsoonal climatic feature.

Accurate simulation of the Indian monsoon’s annual rainfall cycle is essential for applications such as agricultural planning and water resource management by understanding regional climate dynamics. The analysis of annual rainfall cycle (Figure 5) reveals significant variability among models in representing the seasonal distribution of rainfall. Approximately half of the models accurately capture a precipitation peak in July, consistent with observations, while the other half exhibit a delayed peak in August, a common deficiency linked to the excessive persistence of deep convection over the equatorial Indian Ocean, warm SST biases in the eastern Indian Ocean and Bay of Bengal, and a delayed northward migration of the ITCZ (e.g. Sabeerali et al., 2013; Goswami et al., 2019). These biases weaken the early season cross-equatorial moisture transport, suppress June convection, and enhance rainfall later in the season, manifesting as an artificial August intensification. Such errors have been associated with the misrepresentation of monsoon intraseasonal oscillations (MISOs), which govern the northward propagation of convective bands from the equatorial Indian Ocean into the Indian subcontinent (Jiang et al., 2004; Ajayamohan and Goswami, 2007). Another widespread feature across the CMIP6 models is the significant June dry bias, reflecting difficulties in simulating monsoon onset processes, including land-sea thermal contrast development, low-level jet strengthening, and upper-ocean preconditioning. However, the IITM-DCPS provides a realistic representation of the seasonal evolution, showing the smallest June bias among all models. Even the best-performing models from the DCPP (Figure5, EC-Earth3:maroon colour; EC-Earth3-CC:blue dashed line) exhibit moderate June dry bias, whereas the IITM-DCPS captures the onset characteristics more accurately. The suppression of the excessive August rainfall peak in IITM-DCPS is also well comparable with the best DCPP models, indicating improved simulation of ocean-atmosphere coupling, boundary-layer processes, and intraseasonal variability. These improvements reflect the targeted physics upgrades implemented in DCPS, strengthening its ability to capture both the timing and intensity of monsoon rainfall, which is essential for decadal prediction. Nevertheless, IITM-DCPS continues to exhibit a moderate dry bias during the peak monsoon months of JAS. This deficiency is likely linked to the use of simplified microphysics and convection parameterizations with limited hydrometeors which can constrain the intensity and organization of deep convective rainfall and its progression, which is beyond the scope of the present model configuration. It is noteworthy that best performing DCPP models, especially the EC-Earth family, perform well in simulating the mean spatial pattern of monsoon rainfall, also underestimate the rainfall seasonal cycle, underscoring the persistent challenges of simultaneously capturing both spatial climatology and seasonal evolution of the Indian summer monsoon in current-generation climate models.

3.4 Monsoon Indices

The Indian monsoon manifests the dynamic interplay of precipitation and winds, shaping a complex atmosphere-ocean coupled system. Resembling an expansive land and sea breeze analogy, it is driven by the divergent seasonal heating and cooling patterns of continental and oceanic regions. This system encompasses low-level cyclonic vorticity, low level westerly jets, and upper-level anticyclones, forming a deep overturning circulation cell. The dynamics of the monsoon and its interaction with wind patterns are complex processes that manifest in the seasonal reversal of prevailing winds and a pronounced annual precipitation cycle (Goswami & Chakravorty, 2017). This phenomenon is primarily driven by the seasonal fluctuation in land-ocean thermal contrast, influenced by the annual variation of the solar cycle and hemispheric asymmetric SST gradients (Li & Pc., 2018). Moreover, the monsoonal flow can extend into mid-latitudes due to the thermal effects of the elevated Tibetan Plateau. The vertical coupling of upper and lower-level circulations over South Asia is modulated by various external drivers such as the ENSO, impacting the onset and progress of the monsoon (Liu et al., 2015). Consequently, comprehending the complexities of monsoonal dynamics and their interplay with wind fields is imperative for accurately predicting monsoon variability and its associated impacts.

To understand the monsoon dynamics and its “coupling” with the wind fields within our modelling framework, we verify various existing circulation indices that have been proposed in the literature (Webster and Yang, 1992; Goswami et al., 1999; Wang and Fan, 1999; Wilson and Mohanakumar, 2020) with conventional rainfall-based Monsoon indices. Figure 6 represents the time series of simulated Indian Summer Monsoon Rainfall (ISMR) and seasonal mean circulation indices normalised by their own interannual standard deviation for the period of 200 years. The winds used in all circulation indices and rainfall (All India) are averaged over June-September (JJAS) but area-averaged over different regions based on those indices. The pioneering monsoon circulation index, termed Webster Yang Index (WYI) introduced by Webster and Yang (1992), was the first of its kind. It measures the vertical shear of the zonal wind, averaging the mean temporal zonal wind shear between 850 hPa (U850) and 200 hPa (U200). This calculation spans from the Equator to 20°N and covers longitudes 40° to 110°E (Webster and Yang, 1992).

The Monsoon Hadley-circulation Index (MHI) was suggested by Goswami et al. (1999), based on the idea that the regional Hadley circulation arises from the direct influence of the off-equatorial monsoon heat source. This index is determined by the anomaly in meridional wind shear between pressure levels 850 and 200 hPa (V850 -V200), averaged across the area from 70°E-110°E and 10°N-30°N. Wang and Fan (1999) developed another circulation index for the monsoon, known as the Monsoon Circulation Index (MCI), in relation to Convection Index 1 (CI1). CI1 is defined by negative outgoing long-wave radiation (OLR) anomalies averaged over the Bay of Bengal (BOB) region (10°-25°N, 70°-100°E), emphasizing the crucial role of convective latent-heat release in driving summer monsoons. The MCI, recommended for the Indian monsoon, is calculated from the difference between U850 and U200 averaged over the area 5°-20°N, 40°-80°E. A new circulation index, the SMI index, was recently proposed by Wilson and Mohanakumar (2020). This index is a modified version of the MCI index, excluding land regions to minimize topographical effects on zonal wind patterns. It is calculated from the vertical shear of zonal winds between the jet cores of the Low-Level Westerly Jet (ULLJ_core) and Tropical Easterly Jet (UTEJ_core) over the oceanic area 5°-20°N, 50°-70°E. A revised index for the ISM based on the difference in 850 hPa zonal winds between a southern area of 5°S-5°N and 40°-80°E, and a northern area of 20°-30°N and 70°-90°E (HWSI) is developed by Prasad and Hayashi (2007).

The temporal correlations between the circulation indices and ISMR, using normalized time series (JJAS), are calculated for the time period of 200 years and presented in Figure 6. It is noted that the circulation indices correlate strongly with ISMR, with the highest correlation coefficient (CC) found for HWSI (0.83), significant at the 99.9% level, followed by SMI (0.73), and MCI (0.70). The other indices, MHI and WYI, also show significant correlations of 0.68 and 0.56 respectively. The correlation of 0.50 between any index and ISMR suggests that it explains about 25% of the variance of ISMR. The stronger correlations in IITM-DCPS suggest that the model captures the dominant dynamical coupling between large-scale monsoon circulation and rainfall.

Recognizing the crucial influence of the tropospheric temperature gradient (TTG) on ISMR, TTG index (Figure 7) has been calculated by averaging column air temperature from 600 to 200 hPa and taking their difference between the Indian monsoon domain (60-100°E, 20-30°N) and the equatorial region (60-100°E, 5°S-5°N) to quantify its significance, reflecting its role in determining monsoon onset, withdrawal, intensity, regional rainfall distribution, and broader atmospheric dynamics. The onset and withdrawal of the South Asian Monsoon are defined by the TTG shifting from negative to positive and vice versa, driven by adiabatic heating over Asia and Tibetan Plateau warming, with peak positive TTG in July-August due to diabatic cloud heating strengthening monsoon circulation (He et al., 1987; Yanai et al., 1992). Figure 7 reveals a significant correlation (0.52) between the TTG index and ISMR, highlighting the thermodynamic coupling where a strong TTG enhances monsoon circulation through increased moisture convergence and convection, influencing onset timing, rainfall intensity, and regional distribution (Goswami and Xavier, 2005, Xavier et al., 2007). The IITM-DCPS captures the interannual variability of ISMR, with monsoon onset and withdrawal in early June and late September precisely coinciding with the observed TTG gradient reversal.

3.5 Column Integrated Moist Static Energy

Moist Static Energy (MSE) is a crucial parameter in atmospheric thermodynamics that captures the temperature and moisture content of an air parcel and gives information about its potential for energy release and convective activity. The MSE is a measure of total energy that is approximately conserved for hydrostatic, moist adiabatic vertical motions (Adames Corraliza and Mayta, 2023).

$$MSE = C_pT + gz + L_vQ \text{ ---------------------- } (1)$$

where Cp is the specific heat of dry air at constant pressure, T is the temperature, z is the geopotential, g is acceleration due to gravity, Lv is the latent heat of vaporization and Q is the specific humidity.

Monsoon dynamics hinge on the interplay of precipitation, wind patterns, and atmospheric processes, requiring accurate modelling to capture ISM variability. Studies by Wang et al. (2014) and Biasutti et al. (2018) highlight how solar insolation-driven variations in MSE influence seasonal atmospheric circulation and precipitation, with the Himalayan mountains further shaping MSE distribution and modulating monsoon onset and intensity (Boos & Kuang, 2010). Therefore, analyzing the simulated distribution of Vertically Integrated MSE (VIMSE) is critical for refining thermodynamic processes, enhancing the model's prediction of ISM rainfall.

Figure 8 illustrates the comparison of the spatial regression patterns of VIMSE (Jm^{-2}) over the 1000–300 hPa column against ISMR (mm) during the JJAS season between the IITM-DCPS and observation. The IITM-DCPS reasonably captures the spatial distribution of VIMSE, showing increased values over the northern Indian Ocean and western India, consistent with observed patterns, which reflect greater moisture availability and convective activity driving monsoon rainfall. Minor differences, such as slightly weaker VIMSE gradients over the Bay of Bengal in the model, may indicate a possible underestimation of moisture convergence, yet the overall similarity highlights the model's improved depiction of thermodynamic coupling between VIMSE and ISMR, supporting enhanced monsoon circulation as noted in the TTG analysis (Figure 7). Higher VIMSE values correlate with increased ISMR, increasing convective activity and rainfall through enhanced atmospheric moisture availability. This is consistent with the moisture convergence mechanism where moisture-laden air masses converge over the Indian subcontinent to drive convective cloud formation and precipitation.

3.6 Spatial distribution of monsoon intraseasonal Variability

The South Asian summer monsoon rainfall exhibits temporal variability, marked by alternating periods of active and break rainfall (Krishnamurti and Bhalme, 1976; Chen and Chen, 1993; Annamalai and Slingo, 2001; Chatterjee and Goswami, 2004), referred to as the monsoon intraseasonal oscillation (MISO). The MISO accounts for 60% of the ISM variability (Goswami, 2005), plays a pivotal role in modulating the mean monsoon rainfall anomalies and determines whether a particular year experiences excess or deficit conditions. This variability is linked to two distinct atmospheric modes. The first mode, which has a cycle of 10-20 days, moves westward (Krishnamurti and Bhalme, 1976, Chen and Chen, 1993, Annamalai and Slingo, 2001, Chatterjee and Goswami, 2004), while the second mode, with a cycle of 30-60 days, moves northward (Yasunari, 1979, Sikka and Gadgil, 1980, Annamalai and Sperber, 2005, Goswami, 2005). Active rainfall periods bring above-average precipitation, benefiting agriculture and replenishing water reservoirs, but can also lead to floods. Conversely, break rainfall periods result in below-average precipitation, causing droughts that can negatively impact agriculture, water resources, and livelihoods. Thus, the MISO-induced variability in monsoon rainfall can lead to contrasting scenarios of excess or drought years, affecting regional water availability, agricultural productivity, and socio-economic well-being.

In this section we compare the simulation of ISOs by the IITM-DCPS with respect to the observation (Figure 9) by examining the model's ability in representing ISO characteristics over the South Asian region. Spatial patterns of ISO variance reveal prominent activity over the equatorial Indian Ocean, with maxima centered between 5°S–10°N and 60°E–90°E. The 30-60 day band, associated with the Madden–Julian Oscillation (MJO), exhibits substantially higher variance (exceeding 30-40 $(mm/day)^2$) compared to the 10–20 day band (typically 20-25 $(mm/day)^2$). These results highlight the dominance of the MJO in modulating monsoon intraseasonal variability. The enhanced variance near 5°S suggests a convective source region influenced by the Intertropical Convergence Zone (ITCZ) and higher SSTs. Furthermore, the observed northward propagation toward the Indian subcontinent and eastward extension toward the Maritime Continent (90°E–120°E) closely follow established ISO pathways. The IITM-DCPS simulation yields correlation coefficients of $r = 0.81$ and $r = 0.83$ for the 10-20 day and 30-60 day ISOs, respectively, indicating realistic skill in simulating ISO patterns. The IITM-DCPS not only captures the broader eastward extension of ISO variance but also presents smoother spatial gradients, particularly in the 30-60 day band. These results can be attributed to the improved land-atmosphere coupling in reproducing key features of monsoon intraseasonal variability within the decadal prediction system.

3.7 Analysis of Climate Modes of Variability in CMIP6 pi-control runs

CMIP6 pi-control simulations provide a critical framework for isolating the internal variability of the climate system by maintaining fixed atmospheric greenhouse gas concentrations, aerosols, and other external forcings at pre-industrial levels, thus eliminating time-varying anthropogenic influences (Eyring et al., 2016). These simulations enable a detailed examination of intrinsic climate variability of how the ESMs simulate the dominant modes of climate variability such as ENSO, AMO, and PDO. Understanding these modes can help for distinguishing natural climate variability from anthropogenic signals, a key objective of DCPP (Boer et al., 2016).

Our analysis of CMIP6 piControl runs focuses on the decomposition of climate indices to its various modes of variability to evaluate the representation of ENSO, AMO, and PDO, which drive variability across interannual to multidecadal timescales. ENSO, characterized by SST anomalies in the tropical Pacific, is a primary driver of global climate variability, influencing the ISM through teleconnections (e.g. Ashok et al., 2001). However, CMIP6 models often exhibit biases in ENSO amplitude and periodicity (Planton et al., 2021). The AMO, marked by North Atlantic SST fluctuations, impacts mid-latitude and monsoon dynamics, but models frequently struggle to capture its multidecadal periodicity (Zhang et al., 2019). Similarly, the PDO, defined by north Pacific SST patterns, affects regional climate but is often underrepresented in low-resolution models (Newman et al., 2016). In our analysis, we assess the dominant climate modes by decomposing the variance of these key indices across distinct frequency bands. Following this, we evaluate the dominant periodicities driving their variability and assess the fidelity of CMIP6 model simulations, including the IITM-DCPS, in reproducing these patterns.

The variance of each mode is quantified as a percentage of the total variance in the raw signal, with spectral bands categorized by periodicity: the 2-5 year band (interannual (including quasi-biennial variability)), 5-10 year band (near-decadal variability), 10-20 year and 20-40 year bands (decadal), and 40-80 year band (multi-decadal). Figure 10 displays a heat map of variance explained by various frequency bands of climate indices with each cell representing the percentage contribution of the band and model, colour intensity indicating magnitude. This facilitates a comparative evaluation of frequency-dependent variability, using observed spectra in the bottom row as a benchmark for assessing IITM-DCPS performance against other models. Discrepancies between simulated and observed variances identify refinement areas, for the reliability of decadal climate predictions.

The observed percentage of variance of both the ISMR and El Niño show stronger biennial and intra-decadal modes of variability compared to their decadal to multi-decadal counterparts in the original signal over a period of 200 years (Figure 9). The variance of both the interannual-intradecadal modes of ENSO and monsoon is strong and satisfactorily reproduced by all the models as seen in the observations highlighting ENSO as the primary driver of Indian monsoon variability, and with two-way feedback (Goswami et al, 2022) between them at interannual timescales. All the models simulate these modes well, with most of them capturing the associated teleconnections on interannual timescales. Whereas the multidecadal modes of

ENSO are comparatively weak, suggesting its insignificant contribution to the multidecadal variability of the monsoon.

However, the representation of low frequency modes such as PDO and AMO in models varies significantly, some models underestimate the observed variances in their decadal and multi-decadal modes though they represent the variance in interannual-intradecadal modes. Thus, capturing the observed variances of PDO and AMO in models still remains a challenge.

BCC-CSM2-MR captures the observed dominant periodicities of ISMR in the 0–20-year and 50–80-year bands reasonably well, whereas CanESM5 shows notable deviations from these spectral characteristics. Nino3.4 (ENSO) periodicities are well captured in the 2-5 year band by MPI-ESM1-2HR, though MIROC6 deviates towards the 10-20 year band. The observed periodicity of AMO in the 50-80 year band is well represented by some models (e.g. BCC-CSM2-MR), while some models (e.g. FGOALS-f3) show significant variance in the 20-40 year band. Most models captured the 50-80 year band of PDO effectively, though models like MIROC6 show stronger variance in the 10-20 and 20-40 year bands. Overall, the heatmap reveals that while many models capture the dominant periodicities of climate indices well, there are notable discrepancies, particularly in simulating AMO and PDO, highlighting the need for continuous refinement of climate models.

Based on the evaluation across multiple modes (ISMR, Niño3.4, AMO, and PDO) and frequency bands (2-5, 5-10, 10-20, 20-40, 50-80 days), FGOALS-f3 shows better skill among all the models, by capturing the observed variance across various modes and temporal scales. HadGEM3_GC31 also shows high skill, particularly for ISMR and PDO. MIROC6 and MPI-ESM1-2HR show relatively better skills in representing Niño3.4 and PDO features. The IITM-DCPS demonstrated good overall skill, with particularly strong performance in the lower-frequency bands and reasonable agreement with observations across the modes. These results suggest that IITM-DCPS is able to represent several key aspects of climate variability. The analysis further indicates that the model can be applied to studies of monsoon variability, climate teleconnections, and decadal prediction.

3.8 ENSO-monsoon teleconnection at interannual timescales

Earlier studies have demonstrated that on seasonal time scales, the ENSO plays a crucial role in enhancing the skill of precipitation prediction over the tropics (Shukla and Paolino 1983; Wang et al. 2018; Sohn et al. 2019; Dunstone et al. 2020). The ENSO and its teleconnection with the Asian summer monsoon are pivotal elements of global climate variability, significantly influencing regional weather patterns, agricultural practices, ecosystems, and socio-economic structures worldwide. ENSO, distinguished by anomalous warming (El Niño) or cooling (La Niña) of SSTs in the central and eastern equatorial Pacific Ocean, impacts global atmospheric circulation patterns, including the Asian monsoon systems (e.g. Ashok et al., 2007). The well-established and extensively researched teleconnection between ENSO and the Asian monsoon, especially over the Indian subcontinent and Southeast Asia, is noteworthy (Webster et al., 1998).

On interannual timescales, the ENSO-monsoon teleconnection crucially alters the regional precipitation patterns, temperature anomalies, and extreme weather events (Zhang & Sumi, 2002). Comprehending the dynamics and mechanisms of this teleconnection is vital for enhancing seasonal climate predictions, managing disaster risks, and formulating adaptation strategies in susceptible regions. Furthermore, in the context of ongoing climate change, there is a growing interest in evaluating how the ENSO-monsoon teleconnection might transform in a warming world and its potential consequences for regional climate variability and extremes (Wang, 2006).

To evaluate the model's ability in simulating the ENSO phases and capture the global SST distributions, we first constructed composite SST anomalies during the warm and cold events. These composites were based on a 3-month moving average of (December–February, DJF) Niño 3.4 SST anomalies exceeding +0.5 K indicating El Niño conditions, while those below -0.5 K indicating La Niña conditions. Since no annual smoothing was applied to the data, the variability primarily reflects the interannual variability of the ENSO. The IITM-DCPS shows strong agreement with observed SST variability in the eastern Pacific, exhibiting spatial correlations of 0.83 for El Niño conditions and 0.80 for La Niña conditions (Figure 11). The model yields a standard deviation of monthly SST anomalies of 1.03 K, compared to the observed value of 0.78 K. IITM-DCPS's high spatial correlations (0.83 for El Niño, 0.80 for La Niña) with observed SST variability suggest that it effectively captures the spatial patterns of Bjerknes feedback, closely resembling the observed ocean-atmosphere coupling in the eastern Pacific. However, the overestimated standard deviation (1.03 K vs. observed 0.78 K) indicates that the model may amplify the intensity of this feedback, which is common in most of the climate models (Bellenger et al., 2014).

The IITM-DCPS, like many CMIP6 models, exhibits a distinctive feature-a westward extension (~10°E) of the ENSO pattern. This characteristic, while recurrent, serves as an opportunity for continual refinement and enhancement within climate modelling. Researchers have extensively documented this phenomenon (Guilyardi, 2006; Roberts et al., 2018; Van Oldenborgh et al., 2005), presenting avenues for improving model skill and accuracy in simulation and forecasting (Gong et al., 2015; Jiang et al., 2017; Tao et al., 2018; Li et al., 2019). Moreover, understanding and addressing this feature could lead to advancements in predicting shifts in precipitation patterns and atmospheric circulation, fostering more comprehensive climate modelling frameworks (Misra et al., 2007; Ham and Kug, 2015.

The capability of the IITM-DCPS in depicting the simultaneous and delayed teleconnections between ENSO and the monsoon was also assessed. This evaluation was based on a lead-lag correlation analysis involving the Niño3.4 SST and ISMR indices. Figure 12 presents the observed and IITM-DCPS simulated lead/lag relationships between ISMR (JJAS) and monthly Niño3.4 SSTs, spanning from one-year prior (year −1) to one year post (year +1) ISM season (year 0). During ENSO's development stage, warm SST anomalies in the eastern and central Pacific are linked with negative ISMR anomalies, while cold SST anomalies have the opposite effect. This negative correlation gradually fades during ENSO's decay stage. The IITM-DCPS control simulation reproduces not only the significant negative correlation during and after JJAS but also shows a pronounced and highly significant positive correlation (exceeding +0.6) in the pre-monsoon months, indicating a stronger lead-lag relationship with ENSO than observed. Overall, IITM-DCPS slightly overestimates the observed ENSO-monsoon teleconnection, characterized by stronger than observed amplitudes while retaining the correct large-scale coupling structure.

To evaluate the capability of the IITM-DCPS in simulating global precipitation responses to ENSO, composites of mean precipitation were constructed for JJAS season for both El Niño and La Niña years (Figure 13) for the period used for the analysis as shown in Figure 11. During El Niño years, precipitation typically increases over the central and eastern equatorial Pacific, with weak positive anomalies observed over North America and high-latitude regions of South America. Conversely, dry conditions prevail in most land regions, such as Amazon, Australia, South Asia, and the Maritime Continent. The reverse patterns are seen during La Niña years. The primary El Niño and La Niña precipitation patterns over oceans and land are generally well captured by the IITM-DCPS. The pattern correlation between simulated and observed precipitation anomalies is 0.46 and 0.5 for El Niño and La Niña composites, respectively. In addition to tropical precipitation, the model also shows skill in simulating anomalous precipitation patterns in the mid-latitudes.

3.9 IOD and SIOD representation in model.

Accurately capturing the variability of Indian Ocean SST in climate models is important, as it influences the ISM and other climate modes. Several studies reported that the second leading EOF mode of the tropical Indian Ocean SST, the IOD mode, affects ISM independent of ENSO, and it also weakens the ENSO-ISM relation (Ashok et al., 2001; 2004; Cherchi and Navarra, 2013). In addition to the influence on other climate modes, IOD interacts with the subtropical IO SST variability (SIOD) (Cretat et al., 2018) and there is a coupled feedback between IOD and SIOD to enable an internal variability of the Indian Ocean independent from ENSO (Anila and Gnanaseelan, 2023). Therefore, to assess how well the model captures SST variability of tropical and subtropical Indian Oceans is crucial. Here, the EOF modes of tropical and subtropical SST have been compared with observations. EOF analysis shows that the model effectively captures the basin-wide anomalous SST signal associated with the first EOF modes of the tropical Indian Ocean (TIO) and subtropical Indian Ocean (SIO) (Figure 14). However, there's a notable overestimation in the model's representation of SST anomalies over the TIO region, particularly in the eastern TIO area. The model simulates the percentage of variability of the first modes of TIO and SIO SST variability. Moreover, the model simulates the variability of the second mode of the TIO, similar to the observation. While there's a slight overestimation of SST anomalies in both poles of this mode, it is much closer to observations compared to other CMIP6 models. Notably, the unrealistic westward extension of the eastern pole, a characteristic seen in many climate models, is not found in IITM-DCPS. For the second mode of SIO, the percentage of variance is underestimated by the model. The model successfully captures the northeast-southwest dipole structure, a feature that sets it apart from many CMIP6 models that struggle to represent this pattern. The regression analysis on the Niño 3.4 index suggests that the model captures the ENSO-induced SST pattern over TIO and SIO, but underestimates the strength, especially around 20°S.

IOD-monsoon relationship is analyzed by removing the effect of JJAS Niño-3.4 in the simultaneous partial correlations. The correlation between JJAS rainfall and the SST anomalies of the eastern and western IOD boxes are shown in Figure 15. The model overall captures the relationship between SST anomalies over the IOD boxes and the rainfall especially over central India, northwest India, Arabian Sea and western and eastern tropical Indian Ocean regions though there are some discrepancies. This suggests that the model captures the observed IOD monsoon relationship reasonably well, especially in the context of models in general fail to capture the IOD ISMR relationship.

3.10 Evaluation Low-Frequency Climate Modes and its Influence on the Indian Monsoon

3.10.1 Physical Mechanisms and Model Representation of Decadal Climate Modes

The decadal predictability of the climate system arises from the combined influences of the AMO, the PDO, and the decadal modulation of the ENSO itself. The remote influence of the AMO operates through a slow oceanic teleconnection, warm AMO phases generate SST anomalies that are subducted into the North Pacific Subtropical Mode Water (Wu.et.al,2020) and advected over a ~10-12 year pathway (Wu.et.al,2025), eventually re-emerging in the Kuroshio-Oyashio Extension to seed PDO variability (Zhang 2017). Alongside this remote forcing, the PDO is also shaped by decadal ENSO variability, which is characterized by changes in the frequency, intensity, and spatial pattern of El Niño and La Niña events over multi-year timescales (Yeh et al., 2018). This decadal ENSO modulation is driven by oceanic processes within the tropical Pacific, particularly the recharge-discharge cycle of the equatorial heat content and its interplay with the off-equatorial subtropical ocean gyres, which provide a multi-year memory (Dieppois et al., 2021). For example, a shift towards more frequent and intense Central Pacific (CP) El Niño events is a hallmark of a positive PDO phase, as the associated subtropical SST anomalies alter the background state that favours CP El Nino development (Lorenzo et al., 2010). The interplay between these decadal modes can set up large-scale atmospheric wave trains that alter the westerly jet waveguide, inducing significant precipitation anomalies across Eurasia.

The ability of climate models to capture these three interconnected mechanisms the AMO-forced teleconnection, the intrinsic decadal ENSO modulation, and the PDO's teleconnections are critical benchmarks for the decadal predictability. While CMIP models simulate the broad SST patterns of these modes, they often exhibit significant biases in the underlying dynamics. A common failure is the inaccurate representation of the slow oceanic pathway linking the AMO to the Pacific and the thermodynamic feedback governing the decadal ENSO recharge cycle (Smith et al., 2020). These deficiencies contribute to a poor simulation of the observed spectral peak of decadal ENSO mode variability and an unrealistic portrayal of the AMO-PDO phase relationship (Zhang. 2017). Encouragingly, high-resolution models show improved skill in representing the ocean gyre circulations crucial for decadal ENSO and PDO dynamics. However, persistent challenges, such as the spurious strengthening of the Spring Predictability Barrier for CP ENSO in warming scenarios, highlight that accurately simulating the full suite of physical mechanisms remains an ongoing priority for decadal prediction systems (Chen et al., 2024).

3.10.2 Decadal Modulation of ENSO

In addition to its interannual variability, the interdecadal variations of the Indian summer monsoon and tropical SST are also part of a coupled ocean-atmosphere mode, with the ISMR showing strong correlation with ENSO indices (Krishnamurthy & Goswami, 2000). Studies suggest that ENSO’s influence on the monsoon undergoes decadal modulation, likely due to low-frequency climate variability such as the PDO and IPO, which modulate the strength and spatial pattern of ENSO teleconnections (Meehl et al., 2009b; Xiang et al., 2013). During certain decades, the ENSO-monsoon correlation weakens, attributed to shifts in tropical Pacific SST gradients and atmospheric circulation changes (Kumar et al., 1999; Ashok et al., 2004). Furthermore, model simulations indicate that external forcings, including greenhouse gas emissions and aerosols, can contribute to these modulations by altering the background state of the tropical Pacific (Dong & McPhaden, 2017). Understanding this decadal modulation is crucial for improving seasonal and decadal monsoon predictions, as it determines the reliability of ENSO-based forecasting strategies (Goswami et al., 2006).

Figure 16 presents a comparative analysis of SST anomalies associated with the decadal modes of the ENSO, using both observational data and simulations from the IITM-DCPS. The analysis employs Empirical Ensemble Mode Decomposition (EEMD) to extract decadal modes from the Niño 3.4 SST index, a key indicator of ENSO variability. Composite SST anomaly maps are then constructed for both the positive and negative phases of these decadal modes, allowing for a direct comparison between observations and model simulations. Observational data (Fig16: a and b) reveal characteristic ENSO-like patterns, with warm anomalies in the central-eastern equatorial Pacific during the positive phase and cool anomalies during the negative phase. These patterns align with known impacts of the decadal ENSO modes on the ocean-atmosphere system. Meanwhile, the IITM-DCPS simulations (Fig 16: c and d) broadly reproduce these features, capturing the general spatial distribution of SST anomalies. However, noticeable differences exist in the spatial extent and intensity of these anomalies, suggesting potential limitations in the model's representation of decadal ENSO variability.

A closer look at the correlation between observed and simulated SST anomalies further highlights the model's strengths and weaknesses. The correlation coefficients ($r = 0.68$ for the positive phase and $r = 0.71$ for the negative phase) indicate that the model successfully captures a significant portion of the observed variability, though some discrepancies remain. The model's ability to replicate the fundamental structure of ENSO-related SST anomalies suggests that it can be a useful tool for studying decadal climate variability. However, differences in the magnitudes and spatial distributions suggest that further refinements may be needed to improve model performance. Examining the temporal evolution of the decadal ENSO modes and their broader climate impacts plays a crucial role in decadal prediction. Additionally, investigating the underlying mechanisms responsible for model biases could provide insights into how well the IITM-DCPS represents complex ocean-atmosphere interactions. Understanding these strengths and limitations is important for improving decadal climate predictions and enhancing our ability to anticipate long-term climate variability.

The comparative analysis of SST anomalies in the figure 16 (c, d) highlights the ability of IITM-DCPS to capture the spatial patterns associated with decadal ENSO modes. Observational data reveal distinct El Niño- and La Niña-like SST patterns, with warm anomalies in the central-eastern Pacific during the positive phase and cool anomalies during the negative phase. The model generally reproduces these large-scale features, but with some discrepancies in spatial extent and intensity. The correlation coefficients indicate a moderate agreement between observations and simulations, suggesting that while the model captures key aspects of decadal ENSO variability, refinements are needed to improve accuracy. Differences in the representation of SST anomalies could stem from biases in the model's ocean-atmosphere coupling, subgrid-scale processes, or external forcings that are not fully accounted for.

Following the SST analysis, Figure 17 examines the rainfall anomalies during the same composite periods, offering insight into the atmospheric response to decadal ENSO modes. Observations depict a strong relationship between SST and rainfall, with enhanced precipitation over the central-eastern Pacific during El Niño-like conditions and suppressed rainfall in the same region during La Niña-like conditions. The IITM-DCPS captures these broad patterns but exhibits some discrepancies, which are reflected in lower correlation coefficients. This suggests that while the model represents SST-driven anomalies reasonably well, it struggles with accurately simulating precipitation responses, potentially due to biases in atmospheric circulation, convection, or moisture transport. Understanding and improving these limitations is essential for enhancing climate predictions, particularly for assessing the impacts of decadal ENSO variability on regional hydrological cycles.

3.10.3 AMO-monsoon teleconnection

The ISM rainfall exhibits multidecadal variability over the past 200 years, as evidenced by instrumental records. This variability is found to be positively correlated with fluctuations in North Atlantic SSTs, known as the Atlantic Multidecadal Oscillation (AMO) (Lea, 2021). The AMO, a large-scale fluctuation in the SSTs of the North Atlantic Ocean, exhibits a complex relationship with monsoon systems worldwide, particularly the ISM (Goswami et al 2006, Dutta et al, 2024, Zhang et al, 2018). Decadal variations in AMO phases (warm or cold) have been linked to changes in monsoon rainfall patterns, suggesting a teleconnection – a distant atmospheric linkage – between these two climate phenomena. Understanding this AMO-monsoon teleconnection is crucial for improving our ability to predict long-term monsoon variability and its impacts on regional climate and agriculture.

However, the relationship between the AMO and the ISM has been somewhat controversial from a modelling perspective. For instance, analyses of CMIP models from the CMIP3 have yielded conflicting findings, where Ting et al. (2011) reported no discernible connection within control simulations, while some studies suggest that it does not constitute a component of the pure internal variability of the ocean-atmosphere coupled system. This discrepancy highlighted limitations in CMIP3's representation of AMO-ISM teleconnections. Initial research by Luo et al. (2011) revealed a positive correlation between the AMO and ISM in a control simulation using an improved climate Model. As research continues into CMIP5 researchers point out the absence of significant linkage between the AMO and ISM in most models (e.g. Han et al. (2016)). Beyond model-specific differences, the broader discourse considers various climatic forcings such as solar, volcanic, and aerosol effects that further complicate the understanding of their interconnected dynamics. However, recent research by Choudhury et al. (2022) has shed new light on the ISM-AMO relationship. Their analysis of historical simulations spanning CMIP3 to CMIP6 models indicates an evolving perspective. More than half of the models demonstrate the capability to effectively simulate the variance of the AMO, consequently increasing the variance of the ISMR. They also highlight that the ISMR can exhibit multi-decadal variability with faithful variance only if its AMO counterpart demonstrates periodicity between 50 to 80 years and possesses stronger variance, at least greater than 10-20% of its total variance.

From the observational point of view, the North Atlantic SST variability has been reported to be associated with the variability of ISMR on multi-decadal scales (Goswami et al,2006, Wang et al 2009, Zhang. & Delworth 2006) with the North-Atlantic multi-decadal variability, or AMO, potentially influenced by both natural and anthropogenic aerosols. Ocean-atmosphere feedback is found to play a crucial role in modulating this variability, suggesting the AMO's role as an extra-tropical predictable driver for ISMR (Goswami et al 2022), supported by evidence of decadal predictability in North Atlantic climate. The AMO holds a pivotal role in influencing the ISM (Rajesh and Goswami, 2020), as evidenced by the obtained composite SST anomalies during positive (+ve) and negative (-ve) AMO phases.

Here, while investigating the simulated teleconnection between the AMO and the Indian monsoon in the IITM-DCPS, we first extracted the observed and simulated AMO index. The power spectrum analysis reveals that the 65-year mode as seen in the observations are captured by the model with moderate fidelity showing significant variance above the red noise spectrum (Figure 18a,b). This index represents the domain-averaged SST within the North Atlantic region over the region of maximal temperature loading. Subsequently, employing EEMD-based filtering, multi-decadal mode is extracted, and the corresponding positive and negative phases of the AMO are shown in Figure 18c, spanning approximately two centuries of data period with slightly above three AMO cycles. From the decomposed AMO time series of both observations and the model, a regression is performed on the observed and modelled global SSTs to understand the SST loading patterns associated with the AMO. Comparison between observational data and simulations from the IITM-DCPS, as shown in Figure 19, reveals a fair agreement in the patterns of positive and negative SST anomalies. The analysis reveals the model's capability to replicate the observed AMO SST variability over the North Atlantic. Furthermore, extending the investigation to the JJAS rainfall anomalies across the Indian monsoon domain, both observation and IITM-DCPS simulation exhibit contrasting patterns for positive and negative AMO phases.

In observations, the composite rainfall anomalies (both +ve and -ve) exhibit a typical ISO type large-scale horizontal structure (Figure 20), This is because AMO can modulate the clustering of active phases during its positive epochs and clustering of break phases during its negative epochs within the monsoon season, and these modulations lead to an increase or decrease in seasonal mean rainfall (Rajesh and Goswami, 2020) and here we show that the difference between positive and negative composite anomalies represents 10-20% of the variability of the total seasonal mean monsoon rainfall. The model-simulated rainfall anomalies also capture the positive anomalies over the core central Indian domain during the positive epochs and the negative anomalies during the negative epochs of the AMO with 10-15% variability. These further highlights the model's fidelity in capturing the AMO-monsoon teleconnection through a similar active and break clustering mechanism as found in observations. However, there are some discrepancies in the rainfall pattern, possibly due to circulation anomalies associated with the simulated Rossby wave train (Goswami et al, 2022) interconnecting the two. The fidelity of IITM-DCPS in reproducing both the spectral signature and spatial SST patterns of the AMO confirms that the model captures the fundamental dynamics of this low-frequency mode. This capability provides a credible foundation for assessing AMO–monsoon interactions and their role in driving multidecadal ISMR variability a critical step toward identifying sources of decadal predictability.

3.10.4 PDV-monsoon teleconnection

The PDO (Mantua et al., 1997) and its basin-wide counterpart, IPO (Power et al., 1999), represent natural internal variability in the Pacific Ocean at decadal-to-multidecadal timescales, in which, PDO focuses on the North Pacific, IPO encompasses the entire basin (Mantua et al., 1997; Power et al., 1999; Folland et al., 1999; Allan, 2000.). Some researchers refer to this low-frequency variability in the Pacific (PDO), as the SST anomalies in the northern basin during the boreal winter (Mantua et al. 1997; Newman et al. 2016). Both exhibit characteristic patterns of SST anomalies, featuring cold anomalies in the central North Pacific and warm anomalies along the west coast of North America (Mantua et al., 1997; Deser et al., 2004). Several studies highlight the influence of interdecadal variability in the tropical Pacific on global climate, particularly on the ISM (Krishnan and Sugi 2003, Dai, 2013; Dong and Dai, 2015; Villamayor and Mohino, 2015; IPCC, 2007). This interdecadal relationship shows an inverse correlation between Pacific SST fluctuations and ISMR, with warm (cold) phases of Pacific variability corresponding to decreased (increased) monsoon rainfall and vice versa. Additionally, the atmospheric teleconnection patterns indicate a dynamic consistency between Pacific interdecadal variability and atmospheric anomalies over South and Southeast Asia, suggesting significant influence on Indian monsoon dynamics. The IPO does not have a unique frequency that is well-defined, but it shows periodicities in both decadal (15-25 years) and multidecadal (60-70 years) ranges (Minobe 1999; Chao et al. 2000; Tourre et al. 2001; Mantua and Hare 2002; MacDonald and Case 2005).

We define the IPO as the difference between the central-eastern Pacific [150◦ E-150◦ W; 10◦ S-10◦ N] and the tropical central-eastern Pacific [170◦ W- 90◦ W; 25◦ N-45◦ N] SST following Huang et al (2020). Figure 21(a,b) shows the regression pattern of the annual mean SST onto the unfiltered IPO index, illustrating the broad SST response associated with IPO variability (units in K/K). This captures the full spectrum of IPO-related SST variability, including both interannual and decadal timescales. The observed IPO pattern is characterized by significant warm SST anomalies in the tropical Pacific with a characteristic ‘horseshoe ’shape in the North Pacific, similar to an ENSO-like pattern, and extending to the extratropics along the western coasts of the Americas. Two cold SST anomaly tongues are evident in mid-latitudes extending eastward from the coasts of Asia and Oceania. In contrast, Figure 21 (c,d)focuses on the decadal component of the IPO, defined as the 13-year low-pass filtered anomaly of the second EOF of North Pacific SST, following the methodology of Meehl et al. (2016). It displays pattern correlations derived by projecting the smoothed IPO index onto the SST fields from (a) observations and (b) the IITM-DCPS. This comparison highlights the model's capability (r=0.44) in capturing the spatial structure of decadal IPO signals, thereby providing insight into the fidelity of IITM-DCPS in representing low-frequency climate variability linked to the IPO. This suggests that the model reasonably represents the slow oceanic adjustment processes including Rossby wave propagation, thermocline feedbacks, and meridional overturning circulation that govern IPO phase transitions on multidecadal timescales. The influence of Arctic sea ice on the Indian Summer Monsoon Rainfall (ISMR) has been an important area of recent research, and incorporating Arctic sea ice analysis strengthens the relevance of our model evaluation. The IITM-DCPS simulated Arctic sea ice concentration (SIC) across different seasons, with a focus on summer and winter months is compared with the AVHRR observations and the ORAS5 reanalysis dataset in Figure 22. It is important to highlight that the model captures the SIC very well compared to the observation and ORAS5 highlighting its potential to use for different applications.

4.0 Summary and Conclusion

This study comprehensively assesses the performance of the IITM-DCPS in simulating the interannual to decadal variability of the Indian Summer Monsoon (ISM) and its global teleconnections. The evaluation of the IITM-DCPS control experiment shows improvements over the IITM-ESM, particularly in the simulation of key monsoon features and large-scale climate teleconnections. Notably, the IITM-DCPS significantly reduces mid-latitude temperature biases, which have historically affected the accuracy of simulated atmospheric circulation patterns. The model shows enhanced spatial representation of monsoon rainfall. It also captures better the intraseasonal oscillations and tropospheric temperature gradients, both crucial for ISM dynamics.

A major driver of these advancements lies in the incorporation of refined surface-layer physics and updated vegetation and soil classifications, thereby improving land-atmosphere feedback. Combined with the increased horizontal resolution in IITM-DCPS, these upgrades result in a more realistic representation of surface energy balance, near-surface temperature fields, and moisture feedback. Consequently, the improvements seen in both precipitation and temperature fields reflect the combined influence of the updated surface physics and finer spatial resolution, which collectively strengthen the model's predictive capability. Furthermore, the IITM-DCPS shows enhanced skill in capturing key global climate modes such as the ENSO, PDO, and AMO which are fundamental modulators of ISM variability across various timescales. The model shows improved performance in simulating the ENSO-ISM teleconnection, particularly in capturing the lead-lag relationships and the spatial structure of precipitation anomalies. However, some systematic biases such as the westward extension of ENSO-induced SST anomalies still persist.

Beyond interannual variability, the IITM-DCPS also captures low-frequency climate variability more effectively, which is essential for long-term prediction and planning. The model reproduces teleconnections of multi-decadal modes such as the AMO-ISM and PDO-ISM with reasonable accuracy, providing valuable insights into the mechanisms governing monsoon fluctuations on decadal timescales. For instance, the model skillfully simulates the ~65-year periodicity of the AMO and its corresponding rainfall anomalies over the Indian subcontinent. However, some spatial discrepancies particularly in the representation of associated wave patterns and teleconnection structures highlight areas where further model refinement is needed.

Importantly, the model also succeeds in capturing the PDO and IPO impacts on the ISM, demonstrating its capability in analyzing Pacific-driven modulations of monsoon behaviour. This is particularly relevant for understanding the phase-locked behavior of monsoon variability and its relationship with evolving oceanic conditions in the Indo-Pacific region.

In summary, the IITM-DCPS contributes to ongoing efforts in Earth system modeling, with relevance to South Asian monsoon research and decadal climate prediction. Its improved simulation capabilities make it a valuable tool for regional climate projections, long-term risk assessments, and informing climate-sensitive policy decisions. However, the persistence of certain biases such as those related to tropical Indian Ocean SSTs and cloud-aerosol feedbacks indicates the need for continued development. Future research should focus on refining the physical parameterizations related to aerosol-cloud interactions, and an improved land-surface processes to further enhance its predictability.

Acknowledgements

The authors acknowledge the support of the Director of IITM and Secretary of Ministry of Earth Sciences (MoES), Government of India. We also acknowledge Dr. M. Rajeevan, former Secretary, MoES and Prof. Ravi Nanjundiah, former Director, IITM for their help and support in the initial period of development. We also thank CCCR, IITM for sharing the old version of IITM ESM. We thank Dr. P. Swapna, Dr. R. Krishnan and Dr. A.K. Sahai for their support. Simulations were done in Pratyush HPC. We acknowledge the reviewers for their valuable comments and suggestions to improve the report.

References

Adler, R. F., Huffman, G. J., Chang, A., Ferraro, R., Xie, P.-P., Janowiak, J., et al. (2003). The Version-2 Global Precipitation Climatology Project (GPCP) Monthly Precipitation Analysis (1979–Present). Journal of Hydrometeorology, 4(6), 1147–1167. https://doi.org/10.1175/1525-7541(2003)004<1147:tvgpcp>2.0.co;2

Ajibola, F.O., Afolayan, S.A. Impacts of improved horizontal resolutions in the simulations of mean and extreme precipitation using CMIP6 HighResMIP models over West Africa. Environ Monit Assess 196, 328 (2024). https://doi.org/10.1007/s10661-024-12492-7

Alizadeh, O. Advances and challenges in climate modelling. Climatic Change 170, 18 (2022). https://doi.org/10.1007/s10584-021-03298-4

Allan, R. J., 2000: ENSO and Climatic Variability in the Past 150 Years. El Niño and the Southern Oscillation: Multiscale Variability and Global and Regional Impacts, H.F. Diaz and V. Markgraf, Eds., Cambridge University Press.

Anila, S., and C. Gnanaseelan, 2023: Coupled feedback between the tropics and subtropics of the Indian Ocean with emphasis on the coupled interaction between IOD and SIOD. Global and Planetary Change, 223, 104091, https://doi.org/10.1016/j.gloplacha.2023.104091.

Ashok, K., et al., 2001. Impact of the Indian Ocean Dipole on the Relationship between the Indian Monsoon Rainfall and ENSO. Geophysical Research Letters, 28(23), 4499–4502. https://doi.org/10.1029/2001GL013294.

Ashok, K., Z. Guan , N. H. Saji, and T. Yamagata, 2004: Individual and Combined Influences of ENSO and the Indian Ocean Dipole on the Indian Summer Monsoon. Journal of Climate, 17, 3141–3155, https://doi.org/10.1175/1520-0442(2004)017<3141:iacioe>2.0.co;2.

Ashok, K., Z. Guan, N. H. Saji, and T. Yamagata, 2004: Individual and Combined Influences of ENSO and the Indian Ocean Dipole on the Indian Summer Monsoon. Journal of Climate, 17, 3141–3155, https://doi.org/10.1175/1520-0442(2004)017<3141:iacioe>2.0.co;2.

Ashok, Karumuri, S. K. Behera, S. A. Rao, H. Weng, and T. Yamagata, 2007: El Niño Modoki and its possible teleconnection. Journal of Geophysical Research: Oceans, 112, https://doi.org/10.1029/2006jc003798.

Befort, D. J., O'Reilly, C. H., & Weisheimer, A. (2020). Constraining projections using decadal predictions. Geophysical Research Letters, 47(18), e2020GL087900. https://doi.org/10.1029/2020gl087900

Bellenger, H., et al. (2014). ENSO representation in climate models: From CMIP3 to CMIP5. Climate Dynamics, 42(7-8), 1999-2018.

Beusch, L., Gudmundsson, L., and Seneviratne, S. I.: Emulating Earth system model temperatures with MESMER: from global mean temperature trajectories to grid-point-level realizations on land, Earth Syst. Dynam., 11, 139–159, https://doi.org/10.5194/esd-11-139-2020, 2020.
Boer, G. J., Smith, D. M., et al. (2016). The Decadal Climate Prediction Project (DCPP) contribution to CMIP6. Geosci. Model Dev., 9(10), 3751-3777. https://doi.org/10.5194/gmd-9-3751-2016

Bojovic, D., Bilbao R., Leandro, B.D., Markus, D., Pablo, O., Yohan, R. R., Balakrishnan, S.M., Marta, T., Deborah, V., Doblas-Reyes F., (2019), The Biggest unknowns related to Decadal prediction, BAMS, DOI:10.1175/BAMS-D-19-0190.1

Boos, W. R. & Kuang, Z. Dominant control of the South Asian monsoon by orographic insulation versus plateau heating. Nature 463, 218–222 (2010).

Capua, G., et al., 2020. Drivers of Monsoon Variability: A Causal Perspective Using the Circumglobal Teleconnection. Journal of Climate, 33, 1081–1098. https://doi.org/10.1175/JCLI-D-19-0424.1

Carvalho D, Rafael S, Monteiro A, Rodrigues V, Lopes M, Rocha A. How well have CMIP3, CMIP5 and CMIP6 future climate projections portrayed the recently observed warming. Sci Rep. 2022 Jul 14;12(1):11983. doi: 10.1038/s41598-022-16264-6. PMID: 35835803; PMCID: PMC9283450

CCSP, 2008: Climate Models: An Assessment of Strengths and Limitations. A Report by the U.S. Climate Change Science Program and the Subcommittee on Global Change Research [Bader D.C., C. Covey, W.J. Gutowski, I.M. Held, K.E.Kunkel, R.L. Miller, R.T. Tokmakian and M.H. Zhang (Authors)]. Department of Energy, Office of Biological and Environmental Research, Washington, D.C., USA, 124 pp

Chao, Y., M. Ghil, and J. C. McWilliams, 2000: Pacific interdecadal variability in this century's sea surface temperatures. Geophysical Research Letters, 27, 2261–2264, https://doi.org/10.1029/1999gl011324.

Chen, H., Jin, Y., Liu, Z., Liu, C., Wang, Z., & Li, X. (2024). Central-Pacific El Niño-Southern Oscillation less predictable under greenhouse warming. Nature Communications, 15, 4370. https://doi.org/10.1038/s41467-024-48804-1

Cherchi, A., and A. Navarra, 2012: Influence of ENSO and of the Indian Ocean Dipole on the Indian summer monsoon variability. Climate Dynamics, 41, 81–103, https://doi.org/10.1007/s00382-012-1602-y.

Choudhury, B.A., Rajesh, P.V., Zahan, Y. et al. Evolution of the Indian summer monsoon rainfall simulations from CMIP3 to CMIP6 models. Clim Dyn 58, 2637–2662 (2022). https://doi.org/10.1007/s00382-021-06023-0

Crétat, J., B. Pohl, B. Dieppois, S. Berthou, and J. Pergaud, 2018: The Angola Low: relationship with southern African rainfall and ENSO. Climate Dynamics, 52, 1783–1803, https://doi.org/10.1007/s00382-018-4222-3.

Dell'Aquila, A., P. M. Ruti, S. Calmanti, and V. Lucarini (2007), Southern Hemisphere midlatitude atmospheric variability of the NCEP-NCAR and ECMWF reanalyses, J. Geophys. Res., 112, D08106, doi:10.1029/2006JD007376.

Deser, C., Phillips, A., Bourdette, V. et al. Uncertainty in climate change projections: the role of internal variability. Clim Dyn 38, 527–546 (2012). https://doi.org/10.1007/s00382-010-0977-x

Di Capua, G., Kretschmer, M., Donner, R. V., van den Hurk, B., Vellore, R., Krishnan, R., and Coumou, D., 2020: Tropical and mid-latitude teleconnections interacting with the Indian summer monsoon rainfall: a theory-guided causal effect network approach, Earth Syst. Dynam., 11, 17–34, https://doi.org/10.5194/esd-11-17-2020

Dieppois, B., Capotondi, A., Pohl, B., Chun, K., Monerie, P.-A., & Eden, J. (2021). ENSO diversity shows robust decadal variations that must be captured for accurate future projections. Communications Earth & Environment, 2, 212. https://doi.org/10.1038/s43247-021-00285-6

Di Lorenzo, E., Cobb, K., Furtado, J., Schneider, N., Anderson, B., & Bracco, A. (2010). Central Pacific El Niño and decadal climate change in the North Pacific Ocean. Nature Geoscience, 3(11), 762–765. https://doi.org/10.1038/ngeo984

Ding, Q., & Wang, B., 2005. Circumglobal Teleconnection in the Northern Hemisphere Summer. Journal of Climate, 18, 3483–3505. https://doi.org/10.1175/JCLI3473.1

Dong, L., and M. J. McPhaden, 2017: Why Has the Relationship between Indian and Pacific Ocean Decadal Variability Changed in Recent Decades? Journal of Climate, 30, 1971–1983, https://doi.org/10.1175/jcli-d-16-0313.1.

Doblas-Reyes, F., Andreu-Burillo, I., Chikamoto, Y. et al, 2013: Initialized near-term regional climate change prediction. Nat Commun 4, 1715. https://doi.org/10.1038/ncomms2704

Dunstone, N., and Coauthors, 2020: Skilful interannual climate prediction from two large initialised model ensembles. Environmental Research Letters, 15, 094083, https://doi.org/10.1088/1748-9326/ab9f7d.

Dutta, A., Sivankutty, R. & Neena, J.M. Investigating the Atlantic-Indian monsoon teleconnection pathways in PMIP3 last millennium simulations. Clim Dyn 62, 1765–1782 (2024). https://doi.org/10.1007/s00382-023-06994-2

Eyring, V., et al., 2016. Overview of the Coupled Model Intercomparison Project Phase 6 (CMIP6) Experimental Design and Organization. Geoscientific Model Development, 9, 1937–1958. https://doi.org/10.5194/gmd-9-1937-2016

Feba, F., Ashok, K., Collins, M. & Shetye, S.R. Emerging skill in multi-year prediction of the Indian Ocean Dipole. Frontiers in Climate 3, 736759 (2021). https://doi.org/10.3389/fclim.2021.736759

Folland, C. K., D. E. Parker, A. W. Colman, and R. Washington, 1999: Large Scale Modes of Ocean Surface Temperature Since the Late Nineteenth Century. Beyond El Niño, A. Navarra, Ed., Springer Berlin Heidelberg, 73–102.

Fousiya T.S., Gnanaseelan C., Halder S. et al. (2023). A new approach for seasonal prediction using the coupled model CFSv2 with special emphasis on Indian Summer Monsoon. International Journal of Climatology, 43, DOI:10.1002/joc.8126, 4944-4964.

Gadgil, S., et al., 2004. Extremes of the Indian Summer Monsoon Rainfall, ENSO, and Equatorial Indian Ocean Oscillation. Geophysical Research Letters, 31, L12213. https://doi.org/10.1029/2004GL019733

Gong, H., L. Wang, W. Chen, D. Nath, G. Huang, and W. Tao, 2015: Diverse Influences of ENSO on the East Asian–Western Pacific Winter Climate Tied to Different ENSO Properties in CMIP5 Models. Journal of Climate, 28, 2187–2202, https://doi.org/10.1175/jcli-d-14-00405.1.

Goswami, B. N., et al. "Mechanisms for low-frequency variability in the summer monsoon over the Indian region." Geophysical Research Letters 33.4 (2006).

Goswami, B. N., et al., 2006. North Atlantic Oscillation and Indian Summer Monsoon Variability. Climate Dynamics, 26, 703–718. https://doi.org/10.1007/s00382-005-0098-9

Goswami, B. N., Madhusoodanan, M. S., Neema, C. P. & Sengupta, D. A physical mechanism for North Atlantic SST influence on the Indian summer monsoon. Geophys. Res. Lett. 33, L02706 (2006).

Goswami, B., & Chakravorty, S. (2017, April 26). Dynamics of the Indian Summer Monsoon Climate. Oxford Research Encyclopedia of Climate Science. Retrieved 1 May. 2024, from https://oxfordre.com/climatescience/view/10.1093/acrefore/9780190228620.001.0001/acrefore-9780190228620-e-613.

Goswami, B.N. & Xavier, P.K. (2005) ENSO control on the south Asian monsoon through the length of the rainy season. Geophysical Research Letters, 32(18).

Goswami, B.N., Chakraborty, D., Rajesh, P.V. et al. Predictability of South-Asian monsoon rainfall beyond the legacy of Tropical Ocean Global Atmosphere program (TOGA). npj Clim Atmos Sci 5, 58 (2022). https://doi.org/10.1038/s41612-022-00281-3

Goswami, B.N., Krishnamurthy, V. and Annamalai, H. (1999) A broad-scale circulation index for the interannual variability of the Indian summer monsoon. Quarterly Journal of the Royal Meteorological Society, 125(554), 611–633. https://doi.org/10.1256/smsqj.55411.

Goswami, B. B., R. P. M. Krishna, P. Mukhopadhyay, M. Khairoutdinov, and B. N. Goswami, 2015: Simulation of the Indian Summer Monsoon in the Superparameterized Climate Forecast System Version 2: Preliminary Results. J. Climate, **28**, 8988–9012, https://doi.org/10.1175/JCLI-D-14-00607.1.

Griffies, S. M., et al., 2009. Coordinated Ocean-ice Reference Experiments (COREs). Ocean Modelling, 26, 1–46. https://doi.org/10.1016/j.ocemod.2008.08.007

Guillemot H. Climate Models. In: De Pryck K, Hulme M, eds. A Critical Assessment of the Intergovernmental Panel on Climate Change. Cambridge University Press; 2022:126-136.

Guilyardi, E., 2005: El Niño–mean state–seasonal cycle interactions in a multi-model ensemble. Climate Dynamics, 26, 329–348, https://doi.org/10.1007/s00382-005-0084-6.

Ham, Y.-G., and J.-S. Kug, 2015: Improvement of ENSO Simulation Based on Intermodel Diversity. Journal of Climate, 28, 998–1015, https://doi.org/10.1175/jcli-d-14-00376.1.

Han, Z., F. Luo, S. Li, Y. Gao, T. Furevik, and L. Svendsen, 2016: Simulation by CMIP5 models of the Atlantic multidecadal oscillation and its climate impacts. Advances in Atmospheric Sciences, 33, 1329–1342, https://doi.org/10.1007/s00376-016-5270-4.

Hansen, J., et al. (2005), Efficacy of climate forcings, J. Geophys. Res., 110, D18104, doi:10.1029/2005JD005776.

Hausfather, Z., H.F. Drake, T. Abbott, and G.A. Schmidt, 2020: Evaluating the performance of past climate model projections. Geophys. Res. Lett., 47, no. 1, e2019GL085378, doi:10.1029/2019GL085378.

He, H., McGinnis, J.W., Song, Z. & Yanai, M. (1987) Onset of the Asian summer monsoon in 1979 and the effect of the Tibetan Plateau. Monthly Weather Review, 115(9), 1966–1995.

Hersbach, H., Bell, B., Berrisford, P., Hirahara, S., Horányi, A., Muñoz-Sabater, J., et al. (2020). The ERA5 global reanalysis. Quarterly Journal of the Royal Meteorological Society, 146(730), 1999–2049. https://doi.org/10.1002/qj.3803

Hengl, T., et al. (2017). SoilGrids250m: Global gridded soil information based on machine learning. PLoS One, 12(2), e0169748. https://doi.org/10.1371/journal.pone.0169748.

Hirahara, S., Ishii, M., & Fukuda, Y. (2014). Centennial-Scale Sea Surface Temperature Analysis and Its Uncertainty. Journal of Climate, 27(1), 57–75. https://doi.org/10.1175/jcli-d-12-00837.1

Huang, X., and Coauthors, 2020: South Asian summer monsoon projections constrained by the interdecadal Pacific oscillation. Science Advances, 6, https://doi.org/10.1126/sciadv.aay6546.

Hwang, Y., H. Tseng, K. Li, S. M. Kang, Y. Chen, and J. C. H. Chiang, 2021: Relative Roles of Energy and Momentum Fluxes in the Tropical Response to Extratropical Thermal Forcing. J. Climate, **34**, 3771–3786, https://doi.org/10.1175/JCLI-D-20-0151.1.

Hyder, P., Edwards, J., Allan, R.P. et al. Critical Southern Ocean climate model biases traced to atmospheric model cloud errors. Nat Commun **9**, 3625 (2018). https://doi.org/10.1038/s41467-018-05634-2

IPCC, 2021: Climate Change 2021: The Physical Science Basis. Contribution of Working Group I to the Sixth Assessment Report of the Intergovernmental Panel on Climate Change[Masson-Delmotte, V., P. Zhai, A. Pirani, S.L. Connors, C. Péan, S. Berger, N. Caud, Y. Chen, L. Goldfarb, M.I. Gomis, M. Huang, K. Leitzell, E. Lonnoy, J.B.R. Matthews, T.K. Maycock, T. Waterfield, O. Yelekçi, R. Yu, and B. Zhou (eds.)]. Cambridge University Press, Cambridge, United Kingdom and New York, NY, USA, In press, doi:10.1017/9781009157896.

Jiang, W., G. Huang, K. Hu, R. Wu, H. Gong, X. Chen, and W. Tao, 2017: Diverse Relationship between ENSO and the Northwest Pacific Summer Climate among CMIP5 Models: Dependence on the ENSO Decay Pace. Journal of Climate, 30, 109–127, https://doi.org/10.1175/jcli-d-16-0365.1.

Joshi, M. K. & Pandey, A. C. Trend and spectral analysis of rainfall over India during 1901–2000. J. Geophys. Res. 116, D06104 (2011).

Karmacharya, J., Levine, R.C., Jones, R. et al. Sensitivity of systematic biases in South Asian summer monsoon simulations to regional climate model domain size and implications for downscaled regional process studies. Clim Dyn 45, 213–231 (2015). https://doi.org/10.1007/s00382-015-2565-6

Kay, J. E., et al., 2016. The Community Earth System Model (CESM) Large Ensemble Project: A Community Resource for Studying Climate Change in the Presence of Internal Climate Variability. Bulletin of the American Meteorological Society, 97, 1331–1349. https://doi.org/10.1175/BAMS-D-15-00163.1

Kennedy, J. J. (2014), A review of uncertainty in in situ measurements and data sets of sea-surface temperature, Rev. Geophys., 52(3), 1–26, https://doi.org/10.1002/2013RG000434

Kim, H.-M., et al., 2016. MJO Propagation and Its Impact on Indian Monsoon Rainfall in Global Climate Models. Journal of Geophysical Research: Atmospheres, 121, 9223–9240. https://doi.org/10.1002/2016JD024913

Krishnamurthy, V., and B. N. Goswami, 2000: Indian Monsoon–ENSO Relationship on Interdecadal Timescale. J. Climate, 13, 579–595, https://doi.org/10.1175/1520-0442(2000)013<0579:IMEROI>2.0.CO;2.

Krishnamurti, T. N., et al., 2013. Teleconnections of the Indian Summer Monsoon with Global Climate Modes. Meteorology and Atmospheric Physics, 119, 1–15. https://doi.org/10.1007/s00703-012-0219-7

Krishnan, R., and M. Sugi, 2003a: Pacific decadal oscillation and variability of the Indian summer monsoon rainfall. Climate Dynamics, 21, 233–242, https://doi.org/10.1007/s00382-003-0330-8.

Krishnan, R., and M. Sugi, 2003b: Pacific decadal oscillation and variability of the Indian summer monsoon rainfall. Climate Dynamics, 21, 233–242, https://doi.org/10.1007/s00382-003-0330-8.

Krishnan, R., et al., 2009. Monsoon Variability and Its Linkages to Mid-Latitude Circulation. Climate Dynamics, 33, 1099–1116. https://doi.org/10.1007/s00382-008-0479-yLevine, R. C., & Turner, A. G., 2012. Dependence of Indian Monsoon Rainfall on Sea Surface Temperature and Surface Wind. Climate Dynamics, 39, 997–1012. https://doi.org/10.1007/s00382-011-1219-2

Krishnan, R., Sugi, M. Pacific decadal oscillation and variability of the Indian summer monsoon rainfall. Climate Dynamics 21, 233–242 (2003). https://doi.org/10.1007/s00382-003-0330-8

Konda, G., Chowdary, J.S., Gnanaseelan, C. et al. Improvement in the skill of CMIP6 decadal hindcasts for extreme rainfall events over the Indian summer monsoon region. Scientific Reports 13, 21737 (2023). https://doi.org/10.1038/s41598-023-48268-1

Kumar, K. K., B. Rajagopalan, and M. A. Cane, 1999: On the Weakening Relationship Between the Indian Monsoon and ENSO. Science, 284, 2156–2159, https://doi.org/10.1126/science.284.5423.2156.

Kumar, S., Arora, A., Chattopadhyay, R. et al. Seminal role of stratiform clouds in large-scale aggregation of tropical rain in boreal summer monsoon intraseasonal oscillations. Clim Dyn 48, 999–1015 (2017). https://doi.org/10.1007/s00382-016-3124-5

Lea, 2021: The Atlantic Multidecadal Oscillation and Indian summer monsoon variability: a revisit. Indian Summer Monsoon Variability, Elsevier, 353–374.

Li D, Chang P, Yeager SG, Danabasoglu G, Castruccio FS, Small J, Wang H, Zhang Q, Gopal A. The Impact of Horizontal Resolution on Projected Sea-Level Rise Along US East Continental Shelf With the Community Earth System Model. J Adv Model Earth Syst. 2022 May;14(5):e2021MS002868. doi: 10.1029/2021MS002868. Epub 2022 Apr 27. PMID: 35865233; PMCID: PMC9286582

Li, G., and S. Xie, 2014: Tropical Biases in CMIP5 Multimodel Ensemble: The Excessive Equatorial Pacific Cold Tongue and Double ITCZ Problems. J. Climate, **27**, 1765–1780, https://doi.org/10.1175/JCLI-D-13-00337.1.

Li, G., and Coauthors, 2018: Effect of excessive equatorial Pacific cold tongue bias on the El Niño-Northwest Pacific summer monsoon relationship in CMIP5 multi-model ensemble. Climate Dynamics, 52, 6195–6212, https://doi.org/10.1007/s00382-018-4504-9.

Li, T., and P. Hsu, 2017: Monsoon Dynamics and Its Interactions with Ocean. Springer Atmospheric Sciences, Springer International Publishing, 185–229.

Li, T., Hsu, Pc. (2018). Monsoon Dynamics and Its Interactions with Ocean. In: Fundamentals of Tropical Climate Dynamics. Springer Atmospheric Sciences. Springer, Cham. https://doi.org/10.1007/978-3-319-59597-9_6

Lin, QJ., Yu, JY. The potential impact of model horizontal resolution on the simulation of atmospheric cloud radiative effect in CMIP6 models. TAO 33, 21 (2022). https://doi.org/10.1007/s44195-022-00021-3

Liu, B., Wu, G. & Ren, R. Influences of ENSO on the vertical coupling of atmospheric circulation during the onset of South Asian summer monsoon. Clim Dyn 45, 1859–1875 (2015). https://doi.org/10.1007/s00382-014-2439-3

Liu, Y., Donat, M.G., England, M.H. et al. Enhanced multi-year predictability after El Niño and La Niña events. Nature Communications 14, 6387 (2023). https://doi.org/10.1038/s41467-023-42113-9

Ling, F., Luo, J.J., Li, Y., Tang, T., Bai, L., Ouyang, W., Yamagata, T. Multi-task machine learning improves multi-seasonal prediction of the Indian Ocean Dipole. Nature Communications 13, 7681 (2022). https://doi.org/10.1038/s41467-022-35412-0

Luo, F., S. Li, and T. Furevik, 2011: The connection between the Atlantic Multidecadal Oscillation and the Indian Summer Monsoon in Bergen Climate Model Version 2.0. Journal of Geophysical Research, 116, https://doi.org/10.1029/2011jd015848.

Luo, F., S. Li, and T. Furevik, 2011: The connection between the Atlantic Multidecadal Oscillation and the Indian Summer Monsoon in Bergen Climate Model Version 2.0. Journal of Geophysical Research, 116, https://doi.org/10.1029/2011jd015848.

Luo, F., Ying, J., Liu, T. et al. Origins of Southern Ocean warm sea surface temperature bias in CMIP6 models. npj Clim Atmos Sci 6, 127 (2023). https://doi.org/10.1038/s41612-023-00456-6

MacDonald, G. M., and R. A. Case, 2005: Variations in the Pacific Decadal Oscillation over the past millennium. Geophysical Research Letters, 32, https://doi.org/10.1029/2005gl022478.

Mahmood, R., Donat, M. G., Ortega, P., Doblas-Reyes, F. J., & Ruprich-Robert, Y. (2021). Constraining decadal variability yields skillful projections of near-term climate change. Geophysical Research Letters, 48(24), e2021GL094915. https://doi.org/10.1029/2021gl094915

Mantua, N. J., and S. R. Hare, 2002: The Pacific Decadal Oscillation. Journal of Oceanography, 58, 35–44, https://doi.org/10.1023/a:1015820616384.

Mantua, N. J., S. R. Hare, Y. Zhang, J. M. Wallace, and R. C. Francis, 1997: A Pacific Interdecadal Climate Oscillation with Impacts on Salmon Production. Bulletin of the American Meteorological Society, 78, 1069–1079, https://doi.org/10.1175/1520-0477(1997)078<1069:apicow>2.0.co;2.

Meehl, G. A. et al. Decadal climate prediction: An update from the trenches. Bull. Am. Meteorol. Soc. 95, 243–267 (2014).

Meehl, G. A., et al., 2022. The Effects of Bias, Drift, and Trends in Calculating Anomalies for Evaluating Skill of Seasonal-to-Decadal Initialized Climate Predictions. Climate Dynamics, 59, 3373–3389

Meehl, G. A., L. Goddard, J. Murphy, R. J. Stouffer, G. Boer, G. Danabasoglu, K. Dixon, M. Giorgetta, A. Greene, E. Hawkins, G. Hegerl, D. Karoly, N. Keenlyside, M. Kimoto, B. Kirtman, A. Navarra, R. Pulwarty, D. Smith, D. Stammer, and T. Stockdale, 2009: Decadal Prediction: Can it be skillful? Bull. Am. Meteorol. Soc., In press.

Meehl, G., Hu, A., Santer, B. et al. Contribution of the Interdecadal Pacific Oscillation to twentieth-century global surface temperature trends. Nature Clim Change 6, 1005–1008 (2016). https://doi.org/10.1038/nclimate3107.

Merchant, C. J., T. L. Loveland, P. W. Stackhouse, R. W. Saunders, and R. B. Weller (2017), Uncertainty information in climate data records from Earth observation, Earth Syst. Sci. Data, 9(2), 511–532, https://doi.org/10.5194/essd-9-511-2017

Minobe, S., 1999: Resonance in bidecadal and pentadecadal climate oscillations over the North Pacific: Role in climatic regime shifts. Geophysical Research Letters, 26, 855–858, https://doi.org/10.1029/1999gl900119.

Misra, V., and Coauthors, 2007: Validating and understanding the ENSO simulation in two coupled climate models. Tellus A: Dynamic Meteorology and Oceanography, 59, 292, https://doi.org/10.1111/j.1600-0870.2007.00231.x.

Modes and Mechanisms of Internal Variability." National Academies of Sciences, Engineering, and Medicine. 2016. Frontiers in Decadal Climate Variability: Proceedings of a Workshop. Washington, DC: The National Academies Press. https://doi.org/10.17226/23552.

Morales, J.A. (2022). Climate: Climate Variability and Climate Change. In: Coastal Geology. Springer Textbooks in Earth Sciences, Geography and Environment. Springer, Cham. https://doi.org/10.1007/978-3-030-96121-3_24

Morice, C. P., Kennedy, J. J., Rayner, N. A., & Jones, P. D. (2012). Quantifying uncertainties in global and regional temperature change using an ensemble of observational estimates: The HadCRUT4 dataset. Journal of Geophysical Research: Atmospheres, 117(D8), D08101.

Newman, M., and Coauthors, 2016: The Pacific Decadal Oscillation, Revisited. Journal of Climate, 29, 4399–4427, https://doi.org/10.1175/jcli-d-15-0508.1.

Newman, M., et al., 2016. The Pacific Decadal Oscillation, Revisited. Journal of Climate, 29, 4399–4427. https://doi.org/10.1175/JCLI-D-15-0508.1

Niu, G.-Y., et al. (2011), The community Noah land surface model with multi parameterization options (Noah-MP): 1. Model description and evaluation with local-scale measurements, J. Geophys. Res., 116, D12109, doi:10.1029/2010JD015139.

Pai, D. S., M. Sridhar, M. Rajeevan, O. P. Sreejith, N. S. Satbhai, and B. Mukhopadhyay (2014), Development of a new high spatial resolution (0.25° × 0.25°) long period (1901–2010) daily gridded rainfall data set over India and its comparison with existing datasets over the region, Mausam, 65(1), 1–18.

Pasternack, A., Grieger, J., Rust, H. W., and Ulbrich, U., 2021: Recalibrating decadal climate predictions – what is an adequate model for the drift?, Geosci. Model Dev., 14, 4335–4355, https://doi.org/10.5194/gmd-14-4335-2021

Planton, Y. Y., et al., 2021. Evaluating Climate Models' ENSO Simulations in CMIP6. Journal of Climate, 34, 1457–1475. https://doi.org/10.1175/JCLI-D-20-0118.1

Power, S., T. Casey, C. Folland, A. Colman, and V. Mehta, 1999: Inter-decadal modulation of the impact of ENSO on Australia. Climate Dynamics, 15, 319–324, https://doi.org/10.1007/s003820050284.

Prasad, V.S. and Hayashi, T. (2007) Large-scale summer monsoon rainfall over India and its relation to 850 hPa wind shear. Hydrological Processes, 21(15), 1992–1996. https://doi.org/10.1002/hyp. 6707.

Prasanna, V., 2014. Impact of Monsoon Rainfall on the Total Foodgrain Yield over India. Journal of Earth System Science, 123, 1129–1145. https://doi.org/10.1007/s12040-014-0444-x

Rajesh, P.V., Goswami, B.N. Four-dimensional structure and sub-seasonal regulation of the Indian summer monsoon multi-decadal mode. Clim Dyn 55, 2645–2666 (2020). https://doi.org/10.1007/s00382-020-05407-y

Rajeevan, M., J. Bhate, J. D. Kale, and B. Lal (2006), High resolution daily gridded rainfall data for the Indian region: Analysis of break and active monsoon spells, Mausam, 57(1), 1–18.

Rashid, H.A. Factors affecting ENSO predictability in a linear empirical model of tropical air–sea interactions. Scientific Reports 10, 3931 (2020). https://doi.org/10.1038/s41598-020-60371-1

Rayner, N. A., D. E. Parker, E. B. Horton, C. K. Folland, L. V. Alexander, D. P. Rowell, E. C. Kent, and A. Kaplan (2003), Global analyses of sea surface temperature, sea ice, and night marine air temperature since the late nineteenth century, *J. Geophys. Res.*, 108, 4407, doi:10.1029/2002JD002670, D14.

Roberts, C. D., R. Senan, F. Molteni, S. Boussetta, M. Mayer, and S. P. E. Keeley, 2018: Climate model configurations of the ECMWF Integrated Forecasting System (ECMWF-IFS cycle 43r1) for HighResMIP. Geoscientific Model Development, 11, 3681–3712, https://doi.org/10.5194/gmd-11-3681-2018.

Rosenzweig, C., W. Solecki, C. Braneon, P. Racco, G. Mollod, D. Bader, M. Phillips, C. Lang, D. Manley, S. Ali Ibrahim, P. Marcotullio, D. Reckien, A. Ruane, M. De Los Rios White, U. Khalid, A. Ho, T. Gyeong Hamm, A. Jogesh, W. Bugler, E. Jimenez Alonso, G. Wade, A. Rycerz, T. Bailey, M. Berensson, S. Garg, N. Farhad, S. McDaniel, and K. Yilmaz, 2018: The Future We Don't Want: How Climate Change Could Impact the World's Greatest Cities. UCCRN Technical Report. Urban Climate Change Research Network.

Saha, S. K., et al., 2017. Potential Predictability of Indian Summer Monsoon Rainfall in NCEP CFSv2. Journal of Advances in Modelling Earth Systems, 9, 1976–1994. https://doi.org/10.1002/2017MS000966

Sanchez-Gomez, E., Cassou, C., Ruprich-Robert, Y. et al. Drift dynamics in a coupled model initialized for decadal forecasts. Clim Dyn 46, 1819–1840 (2016). https://doi.org/10.1007/s00382-015-2678-y

Schiemann, R., Demory, ME., Mizielinski, M.S. et al. The sensitivity of the tropical circulation and Maritime Continent precipitation to climate model resolution. Clim Dyn **42**, 2455–2468 (2014). https://doi.org/10.1007/s00382-013-1997-0

Shaffrey, L. C., and Coauthors, 2009: U.K. HiGEM: The New U.K. High-Resolution Global Environment Model—Model Description and Basic Evaluation. Journal of Climate, 22, 1861–1896, https://doi.org/10.1175/2008jcli2508.1.

Shukla, J., and D. A. Paolino, 1983: The Southern Oscillation and Long-Range Forecasting of the Summer Monsoon Rainfall over India. Monthly Weather Review, 111, 1830–1837, https://doi.org/10.1175/1520-0493(1983)111<1830:tsoalr>2.0.co;2.

Smith, D.M., Eade, R., Scaife, A.A. et al. Robust skill of decadal climate predictions. npj Climate and Atmospheric Science 2, 13 (2019). https://doi.org/10.1038/s41612-019-0071-y

Smith, D. M., Scaife, A. A., Boer, G. J., Caian, M., Danabasoglu, G., Delworth, T., et al. (2020). North Atlantic climate far more predictable than models imply. Nature, 583(7818), 796–800. https://doi.org/10.1038/s41586-020-2525-0

Stocker, T.F. et.al. (2013): Technical summary. In Climate Change 2013: The Physical Science Basis. Contribution of Working Group I to the Fifth Assessment Report of the Intergovernmental Panel on Climate Change. Cambridge University Press, pp. 33-115, doi:10.1017/CBO9781107415324.005.

Sun, Q., C. Miao, Q. Duan, H. Ashouri, S. Sorooshian, and K. L. Hsu (2018), A review of global precipitation data sets: Data sources, estimation, and intercomparisons, Rev. Geophys., 56(1), 79–107, https://doi.org/10.1002/2017RG000574

Svendsen, Lea. (2021). The Atlantic Multidecadal Oscillation and Indian summer monsoon variability: a revisit. 10.1016/B978-0-12-822402-1.00001-6

Swapna, P., Krishnan, R., Sandeep, N., Prajeesh, A. G., Ayantika, D. C., Manmeet, S., et al. (2018). Long-term climate simulations using the IITM earth system model (IITM-ESMv2) with focus on the South Asian monsoon. Journal of Advances in Modelling Earth Systems, 10, 1127–1149. https://doi.org/10.1029/2017MS001262

Swapna, P., Roxy, M.K., Aparna, K., Kulkarni, K., Prajeesh, A. G., Ashok, K., Krishnan, R.,Moorthi, S., Kumar, A., and Goswami,B.N. (2015). The IITM Earth System Model: Transformation of a Seasonal Prediction Model to a Long-Term Climate Model. Bulletin of the American Meteorological Society 96 (8). doi.10.1175/BAMS-D-13-00276.2

Tao, W., G. Huang, R. Wu, K. Hu, P. Wang, and H. Gong, 2018: Origins of Biases in CMIP5 Models Simulating Northwest Pacific Summertime Atmospheric Circulation Anomalies during the Decaying Phase of ENSO. Journal of Climate, 31, 5707–5729, https://doi.org/10.1175/jcli-d-17-0289.1.

Ting, M., Y. Kushnir, R. Seager, and C. Li, 2011: Robust features of Atlantic multi-decadal variability and its climate impacts. Geophysical Research Letters, 38, n/a-n/a, https://doi.org/10.1029/2011gl048712.

Tourre, Y. M., B. Rajagopalan, Y. Kushnir, M. Barlow, and W. B. White, 2001: Patterns of coherent decadal and interdecadal climate signals in the Pacific Basin during the 20th century. Geophysical Research Letters, 28, 2069–2072, https://doi.org/10.1029/2000gl012780.

Trenberth, K. E., and D. J. Shea (2006), Atlantic hurricanes and natural variability in 2005, Geophys. Res. Lett., 33, L12704, doi:10.1029/2006GL026894.

van Oldenborgh, G. J., S. Y. Philip, and M. Collins, 2005: El Niño in a changing climate: a multi-model study. Ocean Science, 1, 81–95, https://doi.org/10.5194/os-1-81-2005.

Varma, V., et al., 2020. Addressing Southern Ocean Cloud Biases in Climate Models. Geophysical Research Letters, 47, e2020GL087971. https://doi.org/10.1029/2020GL087971.

Varma, V., Morgenstern, O., Field, P., Furtado, K., Williams, J., and Hyder, P.,2020: Improving the Southern Ocean cloud albedo biases in a general circulation model, Atmos. Chem. Phys., 20, 7741–7751, https://doi.org/10.5194/acp-20-7741-2020

Villamayor, J., and E. Mohino, 2015: Robust Sahel drought due to the Interdecadal Pacific Oscillation in CMIP5 simulations. Geophysical Research Letters, 42, 1214–1222, https://doi.org/10.1002/2014gl062473.

W. Zheng, H. Wei, Z. Wang, X. Zeng, J. Meng, M. Ek, K. Mitchell, and J. Derber. Improvement of daytime land surface skin temperature over arid regions in the ncep gfs model and its impact on satellite data assimilation. J. Geophys. Res., 117(D06117), 2012.

Wang, B. and Fan, Z. (1999) Choice of South Asian summer monsoon indices. Bulletin of the American Meteorological Society, 80(4), 629–638. https://doi.org/10.1175/1520-0477 (1999) 080<0629:COSASM>2.0.CO;2.

Wang, B., 2006: The Asian Monsoon. Springer Berlin Heidelberg,.
Wang, Q., Shu, Q., Bozec, A., Chassignet, E. P., Fogli, P. G., Fox-Kemper, B., Hogg, A. McC., Iovino, D., Kiss, A. E., Koldunov, N., Le Sommer, J., Li, Y., Lin, P., Liu, H., Polyakov, I., Scholz, P., Sidorenko, D., Wang, S., and Xu, X., 2024: Impact of increased resolution on Arctic Ocean simulations in Ocean Model Intercomparison Project phase 2 (OMIP-2) , Geosci. Model Dev., 17, 347–379, https://doi.org/10.5194/gmd-17-347-2024

Wang, Y., Li, S. & Luo, D. Seasonal response of Asian monsoonal climate to the Atlantic Multidecadal Oscillation. J. Geophys. Res. Atmos. 114, 1–15 (2009).

Webster, P. J., V. O. Magaña, T. N. Palmer, J. Shukla, R. A. Tomas, M. Yanai, and T. Yasunari, 1998: Monsoons: Processes, predictability, and the prospects for prediction. Journal of Geophysical Research: Oceans, 103, 14451–14510, https://doi.org/10.1029/97jc02719.

Webster, P.J. and Yang, S. (1992) Monsoon and ENSO: selectively interactive systems. Quarterly Journal of the Royal Meteorological Society, 118(507), 877–926. https://doi.org/10.1002/qj. 49711850705.

Wilson, S.S. and Mohanakumar, K. (2020) A new circulation index for the detection of monsoon intensity. International Journal of Climatology, 40(3), 1900–1908. https://doi.org/10.1002/joc.6312.

Wu, B., Lin, X., & Yu, L. (2020). North Pacific subtropical mode water is controlled by the Atlantic Multidecadal Variability. Nature Climate Change, 10(3), 238–243. https://doi.org/10.1038/s41558-020-0692-5

Wu, B., Lin, X., & Yu, L. (2025). Re-emergence memory of subtropical mode-water links Atlantic and Pacific multidecadal variability. National Science Review, 12(5), nwaf047. https://doi.org/10.1093/nsr/nwaf047
Xavier, P.K., Marzin, C. & Goswami, B.N. (2007) An objective definition of the Indian summer monsoon season and a new perspective on the ENSO–monsoon relationship. Quarterly Journal of the Royal Meteorological Society, 133(624), 749–764.

Xiang, B., B. Wang, and T. Li, 2012: A new paradigm for the predominance of standing Central Pacific Warming after the late 1990s. Climate Dynamics, 41, 327–340, https://doi.org/10.1007/s00382-012-1427-8.

Xie, T., Li, J., Chen, K., Zhang, Y. & Sun, C. Origin of Indian Ocean multidecadal climate variability: role of the North Atlantic Oscillation. Clim. Dyn. 56, 3277–3294 (2022).

Yadav, R. K., 2017: Midlatitude Rossby wave modulation of the Indian summer monsoon. Quarterly Journal of the Royal Meteorological Society, 143, 2260–2271, https://doi.org/10.1002/qj.3083.

Yanai, M., Li, C. & Song, Z. (1992) Seasonal heating of the Tibetan plateau and its effects on the evolution of the Asian summer monsoon. Journal of the Meteorological Society of Japan. Ser. II, 70(1B), 319–351.

Yeh, S.-W., Cai, W., Min, S.-K., McPhaden, M. J., Dommenget, D., Dewitte, B., et al. (2018). ENSO atmospheric teleconnections and their response to greenhouse gas forcing. Reviews of Geophysics, 56(1), 185–206. https://doi.org/10.1002/2017RG000568

Zhang, R. & Delworth, T. L. Impact of Atlantic multidecadal oscillations on India/Sahel rainfall and Atlantic hurricanes. Geophys. Res. Lett. 33, L17712 (2006).

Zhang, R., and A. Sumi, 2002: Moisture Circulation over East Asia during El Nino Episode in Northern Winter, Spring and Autumn. Journal of the Meteorological Society of Japan. Ser. II, 80, 213–227, https://doi.org/10.2151/jmsj.80.213.

Zhang, R. (2017). On the persistence and coherence of subpolar sea surface temperature and salinity anomalies associated with the Atlantic Multidecadal Variability. Geophysical Research Letters, 44(14), 7865–7875. https://doi.org/10.1002/2017GL074342

Zhang, R., et al., 2019. A Review of the Role of the Atlantic Multidecadal Oscillation in Atlantic Meridional Overturning Circulation and Associated Climate Impacts. Reviews of Geophysics, 57, 316–375. https://doi.org/10.1029/2019RG000644

Zhang, Z., X. Sun, and X. Yang, 2018: Understanding the Interdecadal Variability of East Asian Summer Monsoon Precipitation: Joint Influence of Three Oceanic Signals. J. Climate, 31, 5485–5506, https://doi.org/10.1175/JCLI-D-17-0657.1.

Zheng, W., Ek, M., Mitchell, K., Wei, H. et al. (2017). Improving the Stable Surface Layer in the NCEP Global Forecast System. Mon. Wea. Rev., 145, 3969–3987. https://doi.org/10.1175/MWR-D-16-0438.1

Figures:

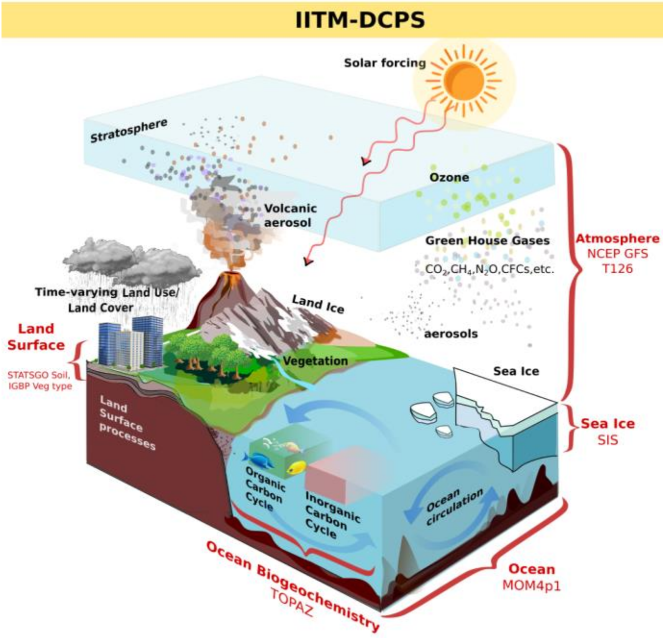

Figure 1*: Schematic of IITM-DCPSv1, highlighting its key physical components, coupled processes, and external forcings used for simulating and predicting climate variability on decadal timescales.*

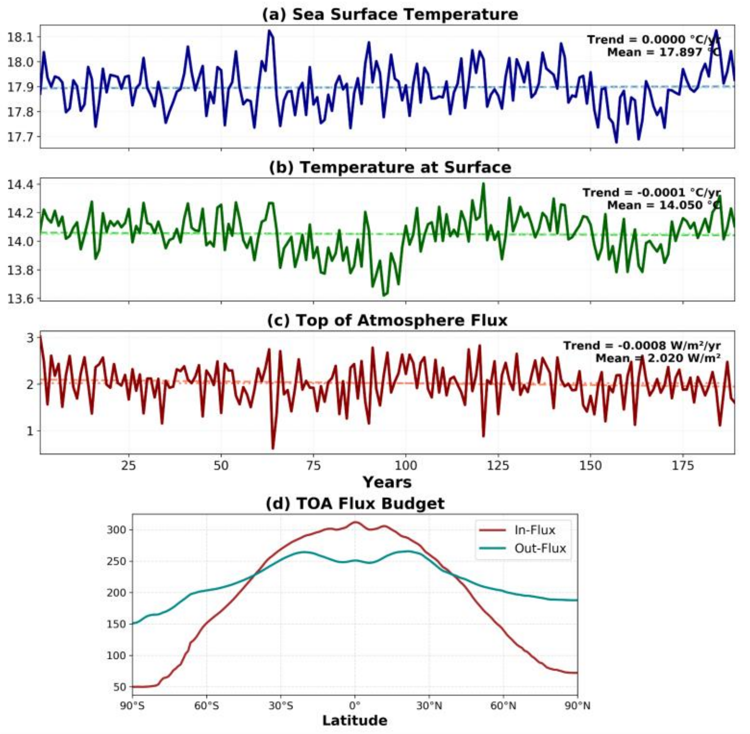

Figure 2: *Time series of annual mean global mean (a) sea surface temperature (SST), (b) surface air temperature (SAT), and (c) top-of-atmosphere (TOA) net radiation and (d) influx and outflux at TOA of the control simulation.*

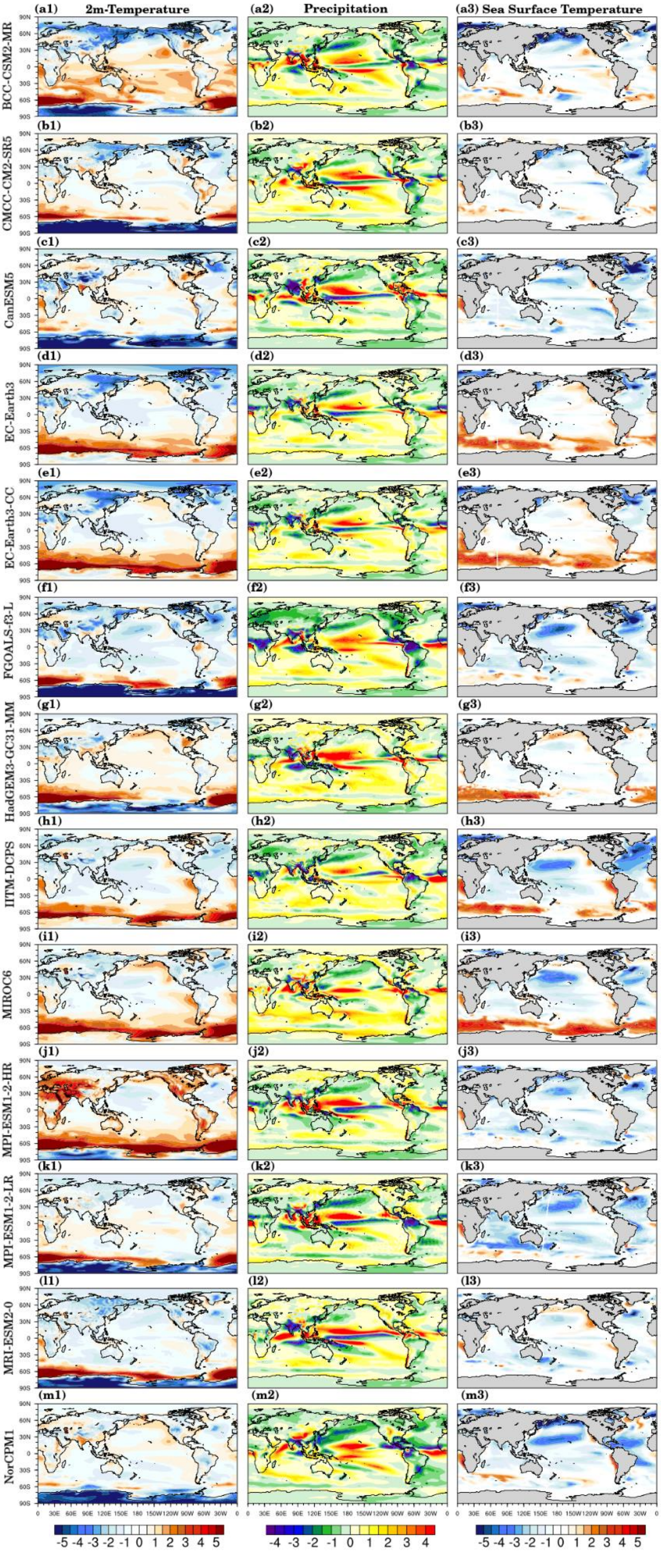
(a1) 2m-Temperature
(a2) Precipitation
(a3) Sea Surface Temperature
BCC-CSM2-MR
(b1)
(b2)
(b3)
CMCC-CM2-SR5
(c1)
(c2)
(c3)
CanESM5
(d1)
(d2)
(d3)
EC-Earth3
(e1)
(e2)
(e3)
EC-Earth3-CC
(f1)
(f2)
(f3)
FGOALS-f3-L
(g1)
(g2)
(g3)
HadGEM3-GC31-MM
(h1)
(h2)
(h3)
IITM-DCPS
(i1)
(i2)
(i3)
MIROC6
(j1)
(j2)
(j3)
MPI-ESM1-2-HR
(k1)
(k2)
(k3)
MPI-ESM1-2-LR
(l1)
(l2)
(l3)
MRI-ESM2-0
(m1)
(m2)
(m3)
NorCPM1
90N
60N
30N
0
30S
60S
90S
0 30E 60E 90E 120E 150E 180 150W 120W 90W 60W 30W 0
-5 -4 -3 -2 -1 0 1 2 3 4 5
-4 -3 -2 -1 0 1 2 3 4
-5 -4 -3 -2 -1 0 1 2 3 4 5

Figure 3: *Bias in 2-meter temperature (first column), precipitation (second column), and sea surface temperature (third column) from 200-year pi-control simulations of 13 Earth System Models (ESMs) participating in CMIP6-DCPP, evaluated against observed climatology. The observed reference climatology for temperature (NCEP-v3) and SST (ERSST-v3) corresponds to the pre-industrial baseline averaged over 1850–1900 (DCPP models), whereas the IITM-DCPS biases are computed relative to the present-day baseline averaged over 1981–2010. Precipitation biases are evaluated using GPCP observations. Each row represents the mean bias for an individual model, with units of °C for 2-meter temperature, mm day^{-1} for precipitation, and K for SST.*

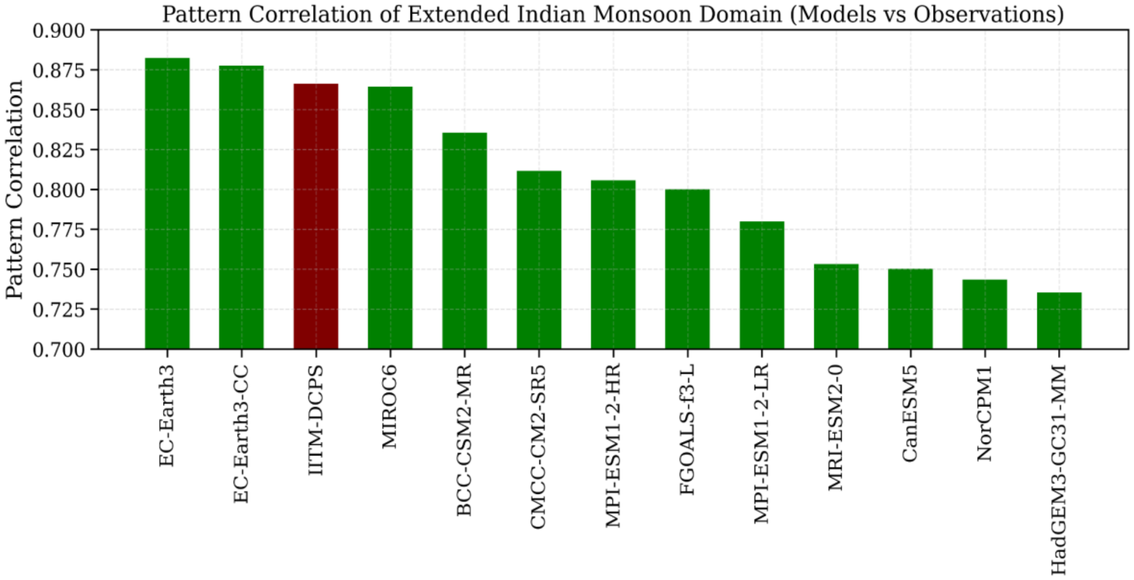

Figure 4: *Pattern correlation of JJAS climatological rainfall over the extended South Asian monsoon domain (40°E-120°E, 10°S-40°N) for various CMIP6 Earth System Models (ESMs) participating in the DCPP, based on their PI-control simulations for 200-year period, compared with observed GPCP rainfall. All other DCPP models are shown in green bars, while IITM-DCPS is represented by the maroon bar.*

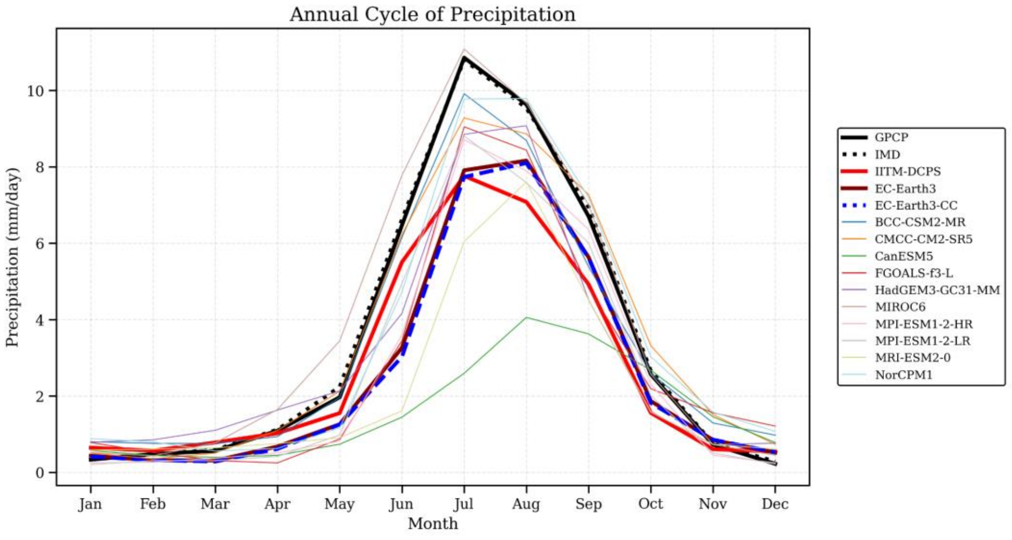

Figure 5: *The annual cycle of all India rainfall from IITM-DCPS (red line), along with PI-*

control runs of various CMIP6 models participating in the DCPP for a period of 200 years, IMD (dotted black line) and GPCP (black line) rainfall.

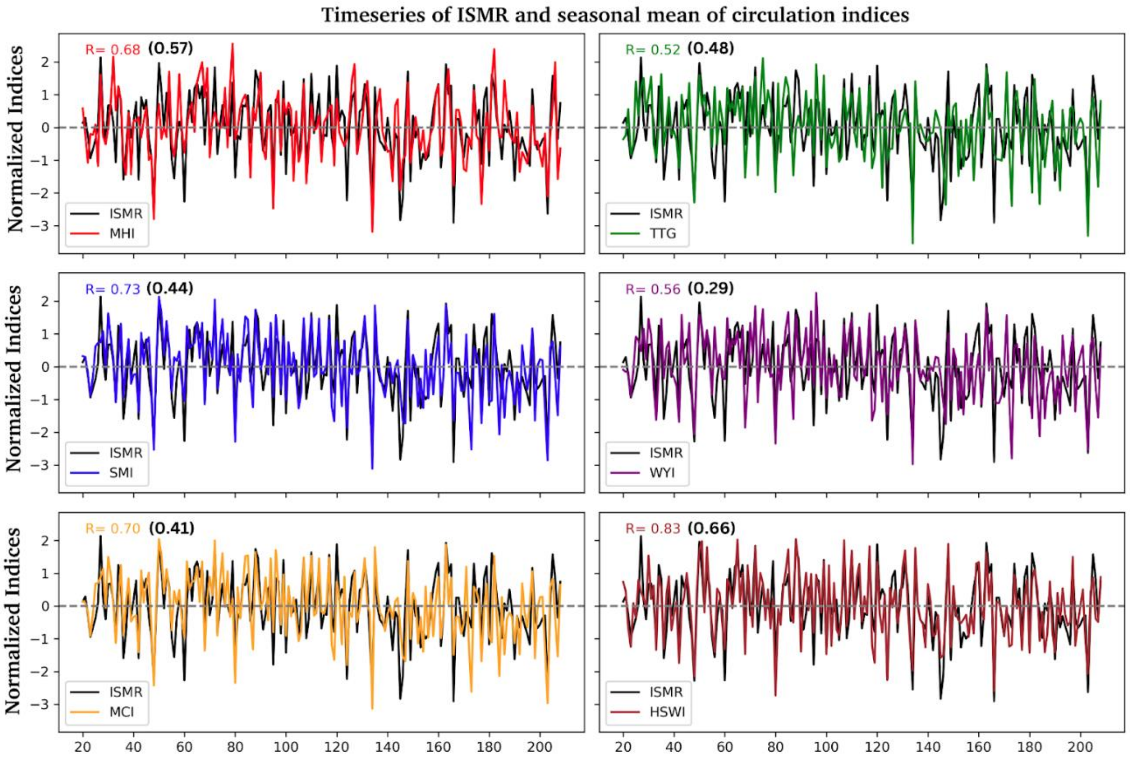

***Figure 6:** Time series of simulated ISMR and seasonal mean circulation indices (MHI, TTG, SMI, WYI, MCI and HWSI) normalized by their own interannual standard deviation for the period of 200 years and the observation. The correlation between ISMR and the respective variables are shown in the respective panels with observed shown in black colour.*

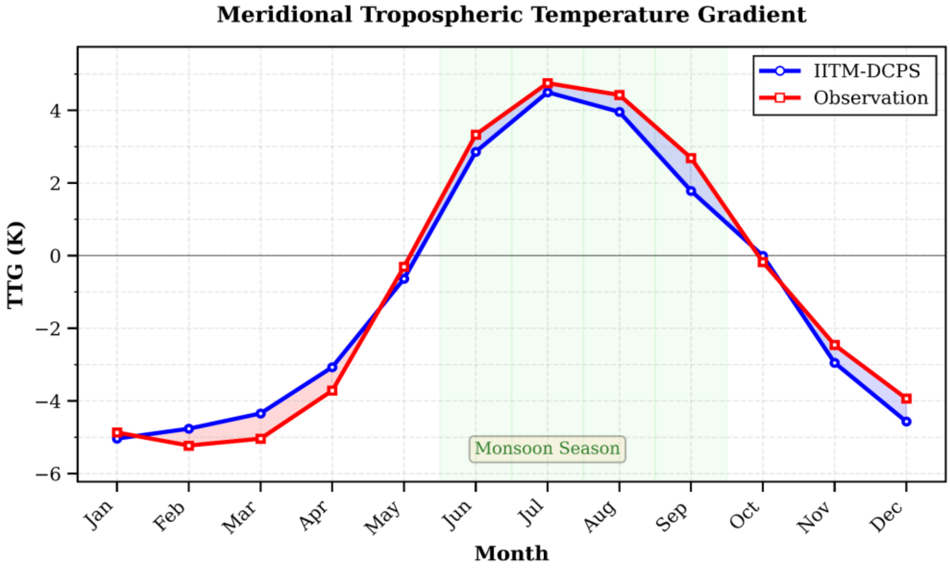

***Figure 7:** Annual cycle of meridional Tropospheric Temperature Gradient (TTG) (deg K) of IITM-DCPS (model) and observation over the period of 200 years. TTG has been calculated by averaging the air temperature over the column 600-200 hPa and taking the difference*

between the Indian monsoon domain (60-100°E, 20-30°N) and the equatorial region (60-100°E, 5°S–5°N). The green shaded monsoon season highlights the period of positive thermal contrast. The shading between the curves denotes systematic model biases, with positive biases shown in red and negative biases in blue.

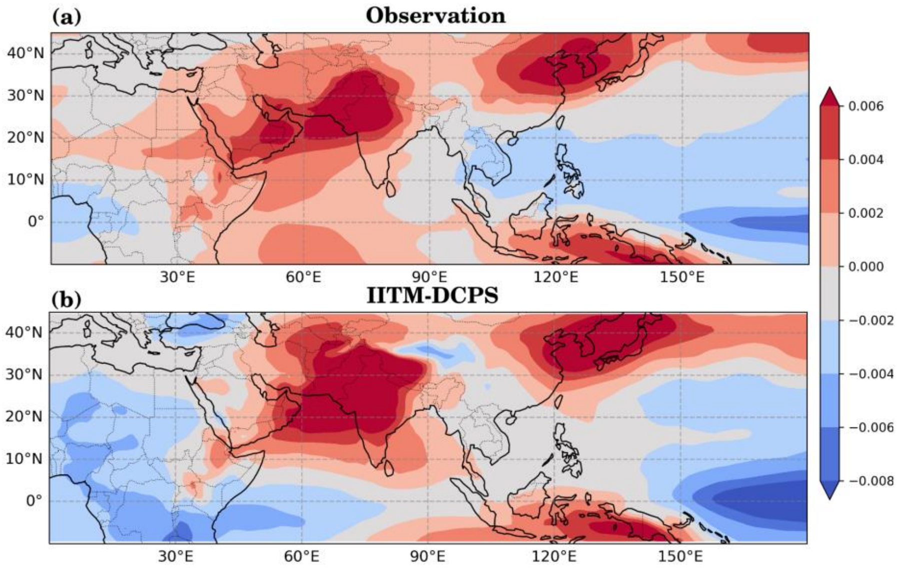

Figure 8: *Spatial distribution of the regression pattern of Vertically Integrated Moist Static Energy (VIMSE, Jm^{-2}) over the column 1000-300hPa, with Indian Summer Monsoon Rainfall (ISMR, mm) during the JJAS season. (a)Observation, (b) IITM-DCPS.*

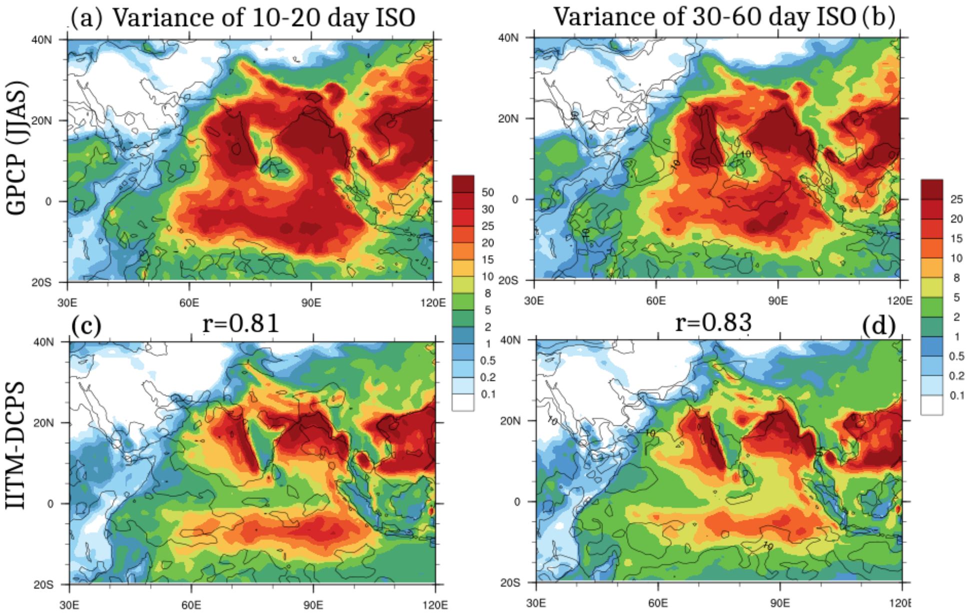

Figure 9: *Variance of the 10–20-day and 30–60-day intraseasonal oscillations (ISOs) for (a, b) GPCP and (c, d) the IITM-DCPS control run respectively. The variance is computed from JJAS daily rainfall filtered ISO components over approximately 30 years for both the model and the observations.*

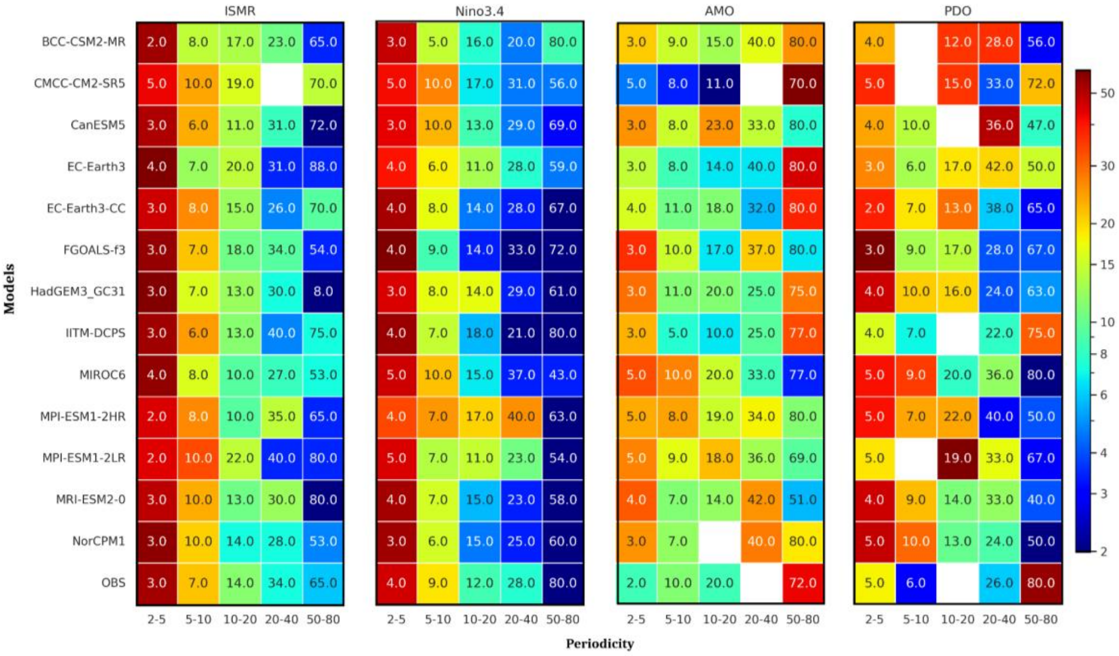

Models	ISMR					Nino3.4					AMO					PDO				
	2-5	5-10	10-20	20-40	50-80	2-5	5-10	10-20	20-40	50-80	2-5	5-10	10-20	20-40	50-80	2-5	5-10	10-20	20-40	50-80
BCC-CSM2-MR	2.0	8.0	17.0	23.0	65.0	3.0	5.0	16.0	20.0	80.0	3.0	9.0	15.0	40.0	80.0	4.0		12.0	28.0	56.0
CMCC-CM2-SR5	5.0	10.0	19.0		70.0	5.0	10.0	17.0	31.0	56.0	5.0	8.0	11.0		70.0	5.0		15.0	33.0	72.0
CanESM5	3.0	6.0	11.0	31.0	72.0	3.0	10.0	13.0	29.0	69.0	3.0	8.0	23.0	33.0	80.0	4.0	10.0		36.0	47.0
EC-Earth3	4.0	7.0	20.0	31.0	88.0	4.0	6.0	11.0	28.0	59.0	3.0	8.0	14.0	40.0	80.0	3.0	6.0	17.0	42.0	50.0
EC-Earth3-CC	3.0	8.0	15.0	26.0	70.0	4.0	8.0	14.0	28.0	67.0	4.0	11.0	18.0	32.0	80.0	2.0	7.0	13.0	38.0	65.0
FGOALS-f3	3.0	7.0	18.0	34.0	54.0	4.0	9.0	14.0	33.0	72.0	3.0	10.0	17.0	37.0	80.0	3.0	9.0	17.0	28.0	67.0
HadGEM3_GC31	3.0	7.0	13.0	30.0	8.0	3.0	8.0	14.0	29.0	61.0	3.0	11.0	20.0	25.0	75.0	4.0	10.0	16.0	24.0	63.0
IITM-DCPS	3.0	6.0	13.0	40.0	75.0	4.0	7.0	18.0	21.0	80.0	3.0	5.0	10.0	25.0	77.0	4.0	7.0		22.0	75.0
MIROC6	4.0	8.0	10.0	27.0	53.0	5.0	10.0	15.0	37.0	43.0	5.0	10.0	20.0	33.0	77.0	5.0	9.0	20.0	36.0	80.0
MPI-ESM1-2HR	2.0	8.0	10.0	35.0	65.0	4.0	7.0	17.0	40.0	63.0	5.0	8.0	19.0	34.0	80.0	5.0	7.0	22.0	40.0	50.0
MPI-ESM1-2LR	2.0	10.0	22.0	40.0	80.0	5.0	7.0	11.0	23.0	54.0	5.0	9.0	18.0	36.0	69.0	5.0		19.0	33.0	67.0
MRI-ESM2-0	3.0	10.0	13.0	30.0	80.0	4.0	7.0	15.0	23.0	58.0	4.0	7.0	14.0	42.0	51.0	4.0	9.0	14.0	33.0	40.0
NorCPM1	3.0	10.0	14.0	28.0	53.0	3.0	6.0	15.0	25.0	60.0	3.0	7.0		40.0	80.0	5.0	10.0	13.0	24.0	50.0
OBS	3.0	7.0	14.0	34.0	65.0	4.0	9.0	12.0	28.0	80.0	2.0	10.0	20.0		72.0	5.0	6.0		26.0	80.0

Figure 10: *Heatmap illustrating the Empirical Mode Decomposition (EMD) variance spectrum, showcasing the variance explained by different modes of climate indices (x-axis) across various climate models (y-axis). The color intensity reflects the relative variance, which is the magnitude of the percentage of variance explained by a specific periodicity band of the original signal, of each climate indices for each model, and the annotations represented by the number inside the matrix shows the dominant periodicity for the respective mode. The observed variances for these indices are depicted in the bottom row of the figure.*

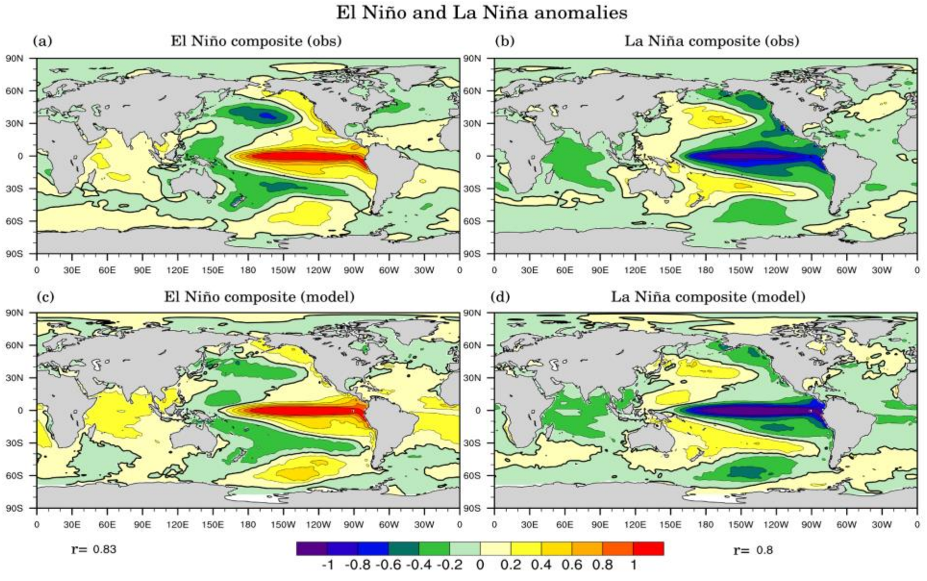

Figure 11: *(a) December–February composites of events with a Niño 3.4 sea surface temperature anomaly greater than 0.5 K (El Niño) and (b) less than 0.5 K (La Niña) after applying a 3-month running mean for sea surface temperature anomaly (K). (c, d), are the same as above, but for IITM-DCPS (model).*

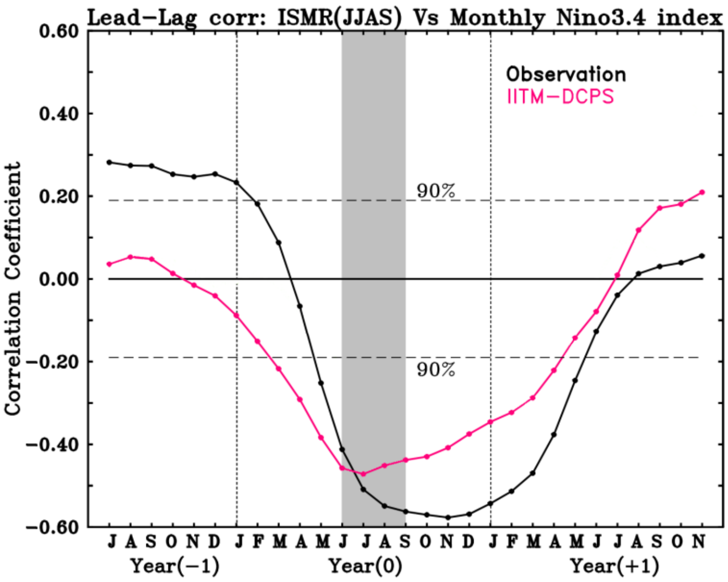

Figure 12: *Lead-lag correlations between Indian monsoon rainfall (JJAS mean) time series (IITM) and monthly Niño-3.4 SST (ERSSTv5) from the previous year (year −1) to the following year of the monsoon (year +1) (Black line). The pink line represents the same analysis using the IITM-DCPS control run. The dashed line denotes 90% confidence level.*

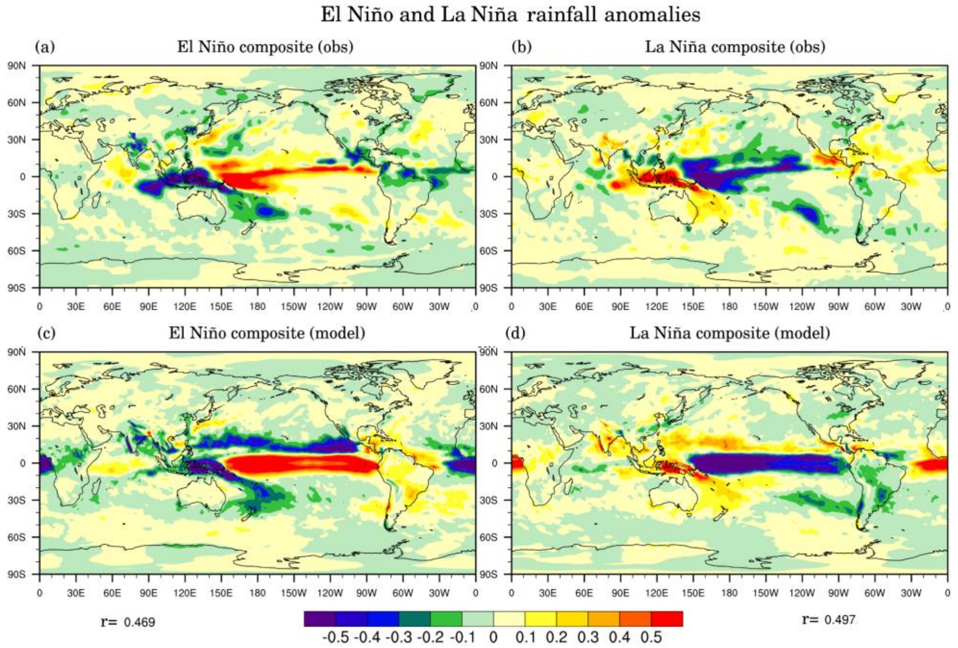

Figure 13: *June–September rainfall anomaly composites of (a) observed El Niño events and (b) observed La Niña events for those years as used as in above Figure 11. (c, d), are the same as above, but for IITM-DCPS.*

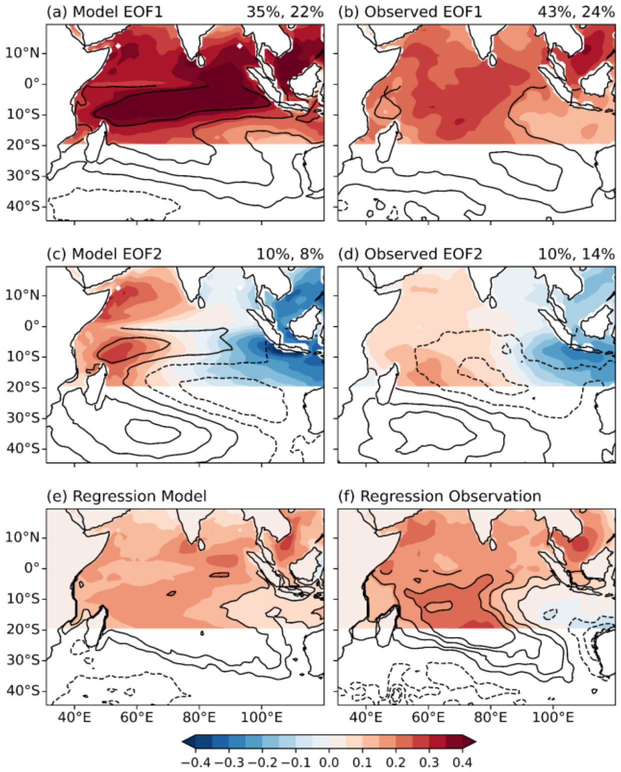

***Figure 14:** (a-b) First and (c-d) second leading EOF modes of SST variability derived from IITM-DCPS and observation over tropical (shaded) and subtropical (contour) Indian Ocean regions. The percentage of variance of the tropical and subtropical EOFs, respectively, are given above the corresponding panel. Regression of Nino 3.4 on tropical (shaded) and subtropical (contour) SST anomalies for (a) model and (b) observation.*

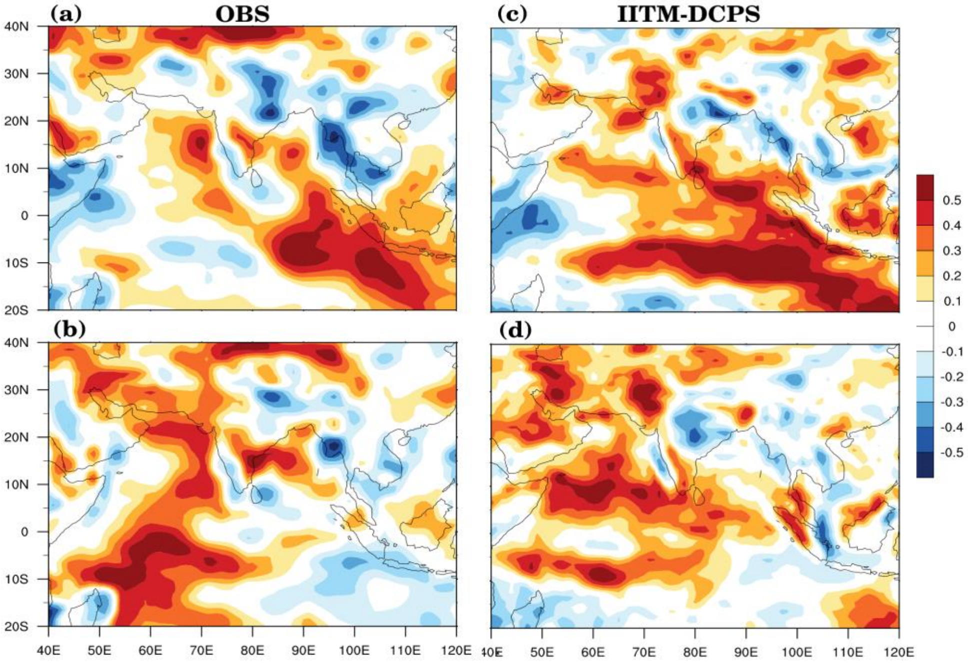

***Figure 15:** Partial correlation between JJAS rainfall with (a, c) JJAS IOD eastern-box SST anomaly and (b, d) JJAS IOD western-box SST anomaly, for observations (left panel) and*

IITM-DCPS (right panel), computed by removing the effect of JJAS Niño-3.4 to isolate the IOD-monsoon relationship.

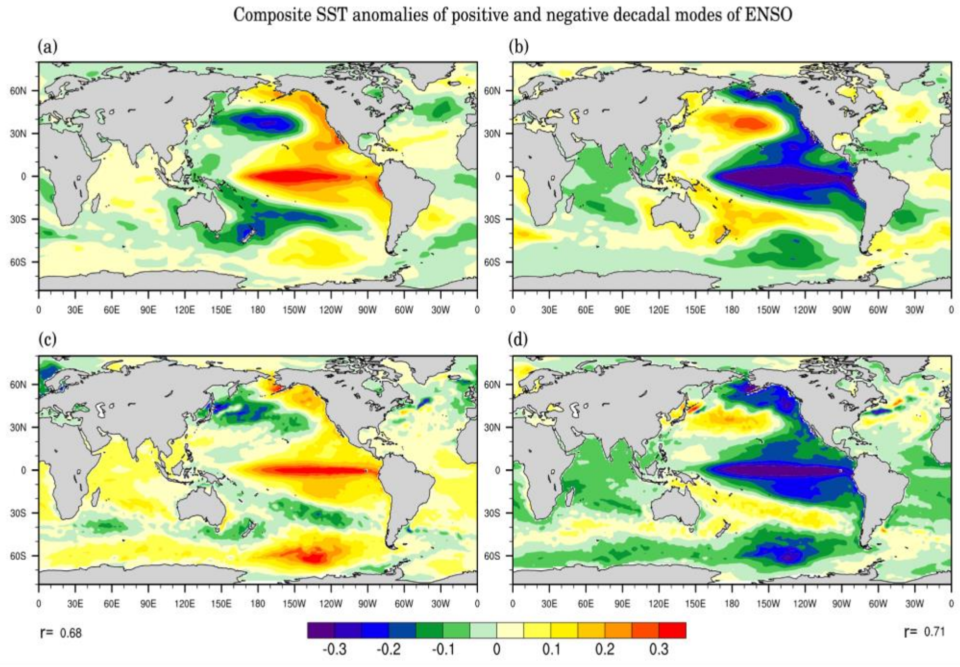

Figure 16: *(a) Composite of SST anomalies for the decadal modes of ENSO positive phases, and (b) depicts ENSO negative phases, derived from observations through EEMD decomposition (combined modes, IMF2 [9yr, variance=18%] and IMF3 [12yr, variance=8%]) of Niño 3.4 sea surface temperature. Similarly, (c, d) present the same analysis for IITM-DCPS (combined modes, IMF2 [9yr, variance=14%] and IMF3 [15yr, variance=4%]).*

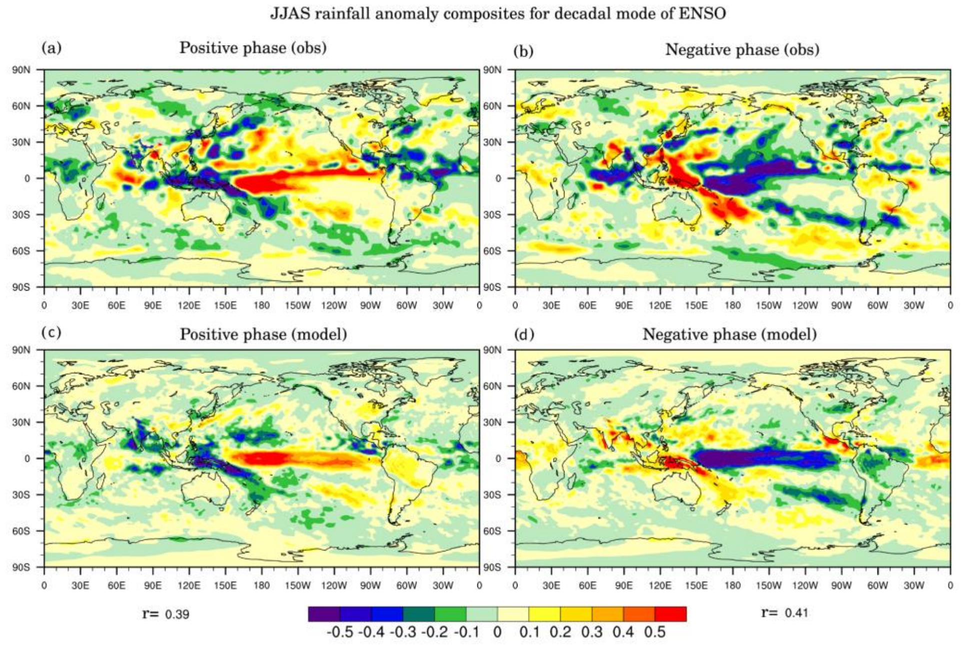

Figure 17: *(a) June-September rainfall anomaly composite for the positive decadal modes of ENSO and (b) for negative decadal modes of ENSO, extracted for the same epochs as illustrated in Figure 16. Similarly, (c, d) present the same analysis for IITM-DCPS.*

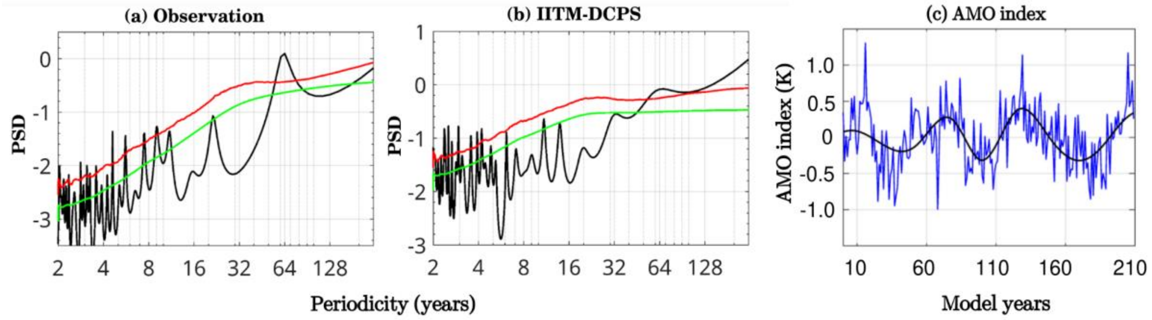

Figure 18: *Power spectra of the AMO index from (a) observations and (b) IITM-DCPS, both derived from the raw non-detrended time series obtained as the domain average SST values over the North Atlantic (NA) (290°E–360°E, 30°N–65°N) domain during boreal summer season, where the maximum SST loading is observed. The significance level bounds of 99% is denoted by red lines, while the green line shows the mean spectrum red-noise modelling.* ***(c)*** *The detrended anomaly time series of the AMO index (blue) from IITM-DCPS over the period of 200-years. The background AMO signal, overlaid on its interannual variability, is decomposed using empirical mode decomposition, shown as the black line.*

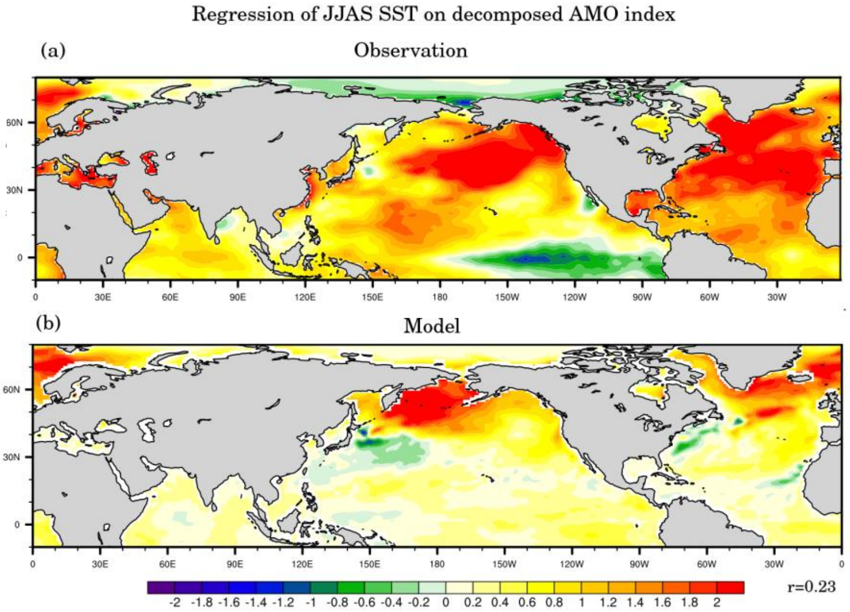

Figure 19: *Regression of the smoothed AMO index using JJAS mean SST for (a) observations and (b) IITM-DCPS (model). This approach generally eliminates the influence of high-frequency variability that helps to bring the background AMO pattern.*

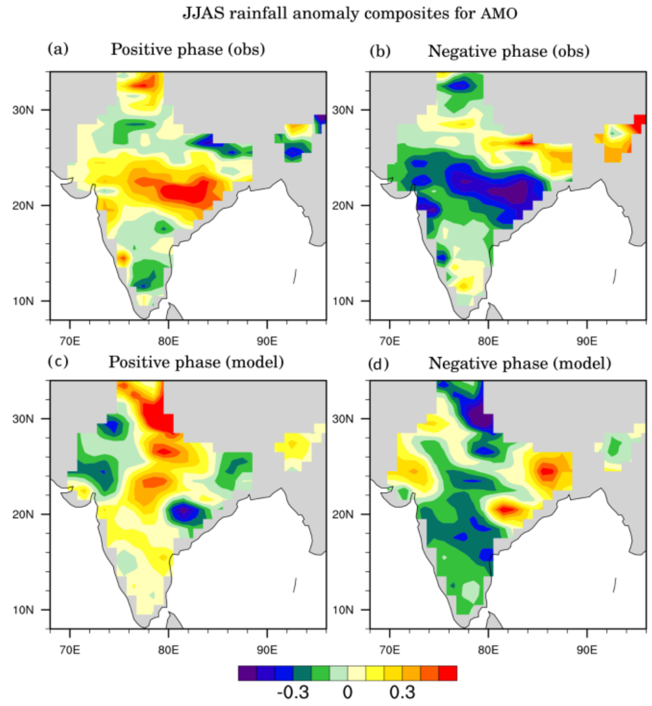

Figure 20: *(a) June–September rainfall Indian monsoon rainfall anomaly composites of (a) positive AMO phases and (b) observed negative AMO phases for those years as used as in above Figure 13. (C, d), are same as above, but for IITM-DCPS.*

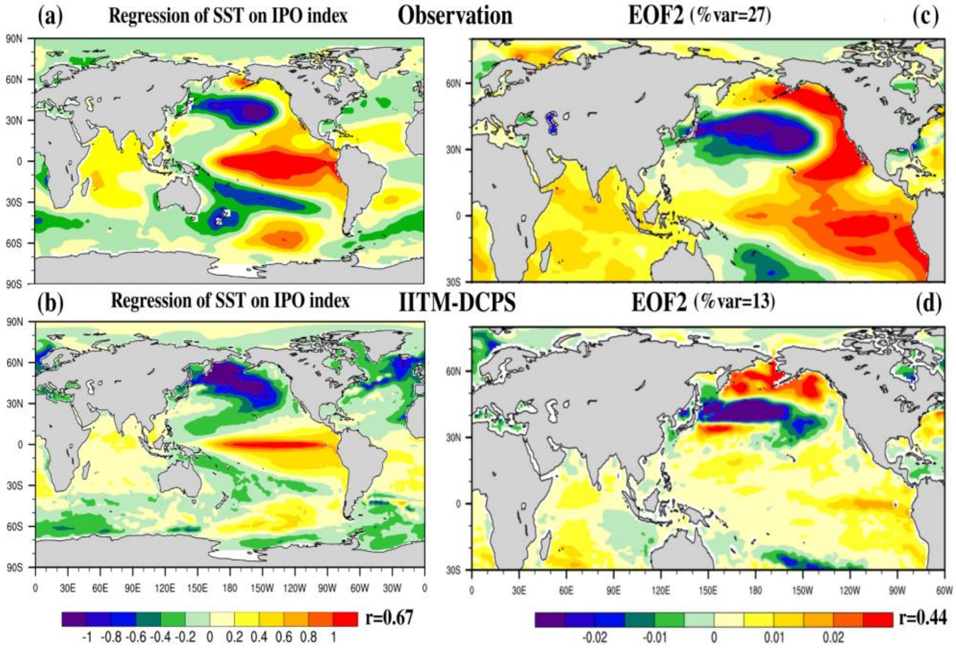

Figure 21: *Regression pattern of the annual mean SST onto the unfiltered IPO index (units are K/K) (a) observation (b) IITM-DCPS (model). Pattern correlations from projecting the smoothed IPO index onto the SST of (c) observation and (d) IITM-DCPS, referred to as the decadal component of the IPO. The decadal component of the IPO is defined as the 13-year low-pass filtered anomaly of the second EOF of NP SST, following the method from Meehl et al., 2016.*

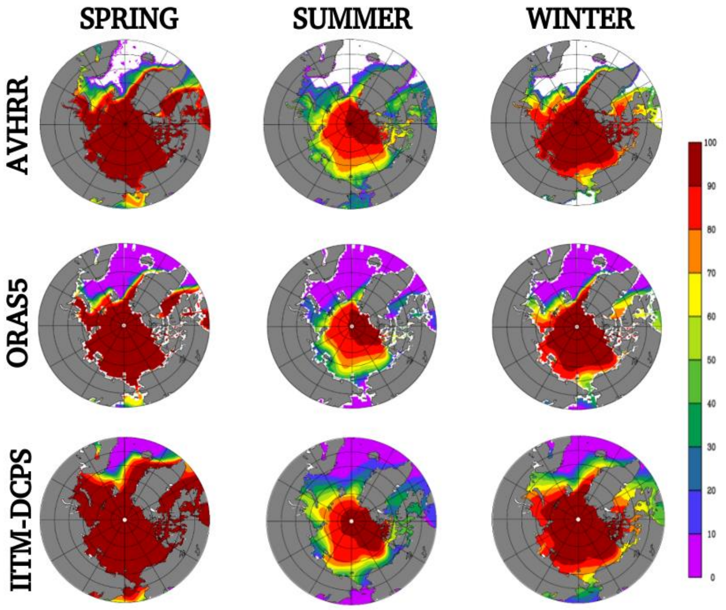

Figure 22: *Seasonal climatology of Arctic sea ice concentration (SIC) from (a) AVHRR observations, (b) ORAS5 reanalysis, and (c) IITM-DCPS model simulation. Panels from left to right represent spring, summer and winter seasons.*